

Summer 2021

A Semi-Active Vibration Isolator For 3D Printing On Shipboard

Mohammad Z. Shahabuddin

Follow this and additional works at: <https://digitalcommons.georgiasouthern.edu/etd>



Part of the [Tribology Commons](#)

Recommended Citation

Shahabuddin, Mohammad Z., "A Semi-Active Vibration Isolator For 3D Printing On Shipboard" (2021). *Electronic Theses and Dissertations*. 2303.
<https://digitalcommons.georgiasouthern.edu/etd/2303>

This thesis (open access) is brought to you for free and open access by the Graduate Studies, Jack N. Averitt College of at Digital Commons@Georgia Southern. It has been accepted for inclusion in Electronic Theses and Dissertations by an authorized administrator of Digital Commons@Georgia Southern. For more information, please contact digitalcommons@georgiasouthern.edu.

A SEMI-ACTIVE VIBRATION ISOLATOR FOR 3D PRINTING ON SHIPBOARD

by

MOHAMMAD SHAHABUDDIN

(Under the Direction of Sevki Cesmeci)

ABSTRACT

In the recent years, additive manufacturing (AM) (*aka 3D printing*) has become a viable alternative to traditional manufacturing due to its unique advantages, such as enabling the fabrication of complex geometries at reduced weight and costs as well as allowing on-site fabrication for maintenance and repair. One specific application area of AM is with navy vessels. During extended voyages, the navy vessels likely require the convenience of on-site fabrication of the malfunctioned parts. However, the shipboard equipment suffers from a broad range of external excitations arising not only from the waves but also from the vessel's engines, which poses a concern for the quality of the 3D printed parts. Thus, efficient vibration isolation systems are needed for quality production. To this end, in this study, a novel semi-active vibration isolation system called Magnetorheological-based Semi-Active Vibration Isolator (MR-SAVI) was proposed. A comprehensive design methodology for the MR-SAVI, including both analytical and simulation modeling, was presented. A sophisticated optimization program was created to find the optimal values of the significant design parameters. The results were discussed, and future recommendations were made for the fabrication and characterization of the device.

INDEX WORDS: Magnetorheological, Magnetorheological fluid, Magnetorheological elastomer,
Vibration isolator, Structural control, Semi-active control

A SEMI-ACTIVE VIBRATION ISOLATOR FOR 3D PRINTING ON SHIPBOARD

by

MOHAMMAD SHAHABUDDIN

Bachelor of Science, University of South Florida, 2019

A Thesis Submitted to the Graduate Faculty of Georgia Southern University in Partial

Fulfilment of the Requirement for the Degree

MASTER OF SCIENCE

© 2021

MOHAMMAD SHAHABUDDIN

All Rights Reserved

A SEMI-ACTIVE VIBRATION ISOLATOR FOR 3D PRINTING ON SHIPBOARD

by

MOHAMMAD SHAHABUDDIN

Major Professor: Sevki Cesmeci
Committee: Mahmoud Baniyadi
Jinki Kim

Electronic Version Approved:
July 2021

DEDICATION

I humbly dedicate my work to my loving parents, whose affection, love, and encouragement make me able to get such success and honor, to my brothers and sisters for always loving and supporting me.

ACKNOWLEDGMENTS

Praise be to God. A special feeling of gratitude and appreciation to my advisor and committee chair, Dr. Sevki Cesmeci, for the support and guidance he has provided throughout this study, without which this research would not have been possible.

I would also like to thank my committee members, Dr. Mahmoud Baniyadi and Dr. Jinki Kim, for serving as my committee members. I also want to thank you for your brilliant comments and suggestions, thanks to you.

I would especially like to thank Mechanical Engineering Lab Supervisor at Georgia Southern, Jeffrey Hoopes for the efforts you put in to help us with this work.

I would also like to acknowledge the students, Anthony Palacio, and Austin Robbins, with whom I worked on a number of projects.

I would like to acknowledge the funding and facilities provided by the Department of Mechanical Engineering at Georgia Southern University.

TABLE OF CONTENTS

ACKNOWLEDGMENTS	3
LIST OF TABLES	6
LIST OF FIGURES	7
CHAPTER 1	9
INTRODUCTION	9
1.1 Hypothesis	11
1.2 Objectives	11
CHAPTER 2	12
LITERATURE REVIEW	12
2.1 Overview	12
2.2 Additive Manufacturing	12
2.3 Structural Control System	13
2.3.1 Active Isolation Systems	14
2.3.2 Passive Isolation Systems	14
2.3.3 Semi-Active Isolation Systems	15
2.4 Magnetorheological Vibration Isolators	18
2.4.1 Magnetorheological Fluid	19
2.4.2 Magnetorheological Elastomer	20
CHAPTER 3	24
METHODOLOGY	24
3.1 Overview	24
3.2 Analytical Modeling	29
3.2.1 Viscous Damping Force	30

3.2.2 MR Damping Force	31
3.3 Finite Element Modeling	32
3.3.1 Electromagnetic Analysis	33
3.3.2 Thermal Analysis	34
CHAPTER 4	37
RESULTS AND DISCUSSION	37
4.1 Electromagnetic Analysis Results.....	37
4.2 Thermal Analysis Results	42
4.3 Optimization	43
CHAPTER 5	48
SUMMARY AND CONCLUSIONS	48
5.1 Conclusion	48
5.2 Future work.....	49
REFERENCES	50
APPENDICES	57
APPENDIX A. PISTON RIGHT END TECHNICAL DRAWING OF THE MR-SAVI.....	57
APPENDIX B. PISTON LEFT END TECHNICAL DRAWING.....	58
APPENDIX C. PISTON BODY TECHNICAL DRAWING	59
APPENDIX D. PISTON ASSEMBLY TECHNICAL DRAWING.....	60
APPENDIX E. CYLINDER RIGHT SIDE TECHNICAL DRAWING	61
APPENDIX F. CYLINDER LEFT SIDE TECHNICAL DRAWING	62
APPENDIX G. CAP LEFT SIDE TECHNICAL DRAWING	63
APPENDIX H. CAP RIGHT SIDE TECHNICAL DRAWING	64

LIST OF TABLES

Table 1: Design requirements for MR-SAVI.....	27
Table 2: Obtained Optimized input and output parameters	47

LIST OF FIGURES

Figure 1: Overview of the typical additive manufacturing workflow: (a) turning an idea into a drawing using CAD, (b) preprocessing of model data, and (c) a digital model is turned into a physical object by adding material a layer at a time (Clark, Liska, and Mülhaupt 2017).	13
Figure 2: Kajima Shizuoka Building and Semi-active Hydraulic Damper (Kobori 2000)	17
Figure 3: Maximum Responses (El Centro, Taft and Hachinohe Waves with 50 cm/sec and Assumed Tokai Waves) (Soong and Spencer 2000).....	17
Figure 4: Structure with Semi-active Control (Soong and Spencer 2000).....	18
Figure 5: Typical MR damper components (Poynor and Reinholtz 2001)	19
Figure 6: Activation of MR fluid: (a) no magnetic field applied; (b) magnetic field applied; (c) ferrous particle chains have formed (© 2005 Lord Corporation All rights reserved)	20
Figure 7: Schematic diagram of fabrication process of isotropic and anisotropic MREs (Kwon, Lee, and Choi 2018)	21
Figure 8: Schematic illustration for printing of hybrid MRE via extrusion printing (Bastola, Paudel, and Li 2018)	23
Figure 9: (a) Isometric cross-section view of the MR-SAVI and (b) detailed view demonstrating the generated magnetic flux lines in the flow gap.	25
Figure 10: The significant geometric design parameters. (a) 2D cross-section of the MR-SAVI and (b) detail view of the top part of the device where contains the MR fluid.	26
Figure 11: The schematic diagram for the Design Methodology of MR-SAVI	29
Figure 12 : Graphical representation of the Bingham plastic model (Cesmececi 2017)	31

Figure 13: (a) CAD model cross section view of MR-SAVI (b) magnetic flux density distribution B magnitude using Maxwell 2D, (c) B vector using Maxwell 3D vector in electromagnetic analysis with current input of 1000 A.....	37
Figure 14: Variation of dynamic force range, D, with respect to the (a) flow gap, (b) active pole length, (c) passive pole length.....	39
Figure 15: Variation of of viscous damping ratio, $\zeta_{viscous}$, with respect to the (a) flow gap, (b) active pole length, (c) passive pole length.....	42
Figure 16: Transient Thermal analysis.....	43
Figure 17: A multi-objective optimization program developed in ANSYS platform.....	44
Figure 18: Optimization input parameters	45
Figure 19: Optimization output parameters	46

CHAPTER 1

INTRODUCTION

As an exciting and still evolving technology, 3D printing has gained increasing popularity in recent years due to its effectiveness, particularly in prototyping, maintenance, repair, and direct production in some cases. Additive manufacturing (AM) can be utilized for various purposes and applications such as prototyping, end-products in medical, aerospace, automotive industries at any location. (Campbell et al. 2011). One of the immediate applications of this technology is its use in military applications. This technology can be adopted for various military projects, and many military branches are calling for more adoption of additive manufacturing; one specific use is in the navy. The United States Navy started adding 3D printers to some of their vessels. The very first 3D printer has been installed onboard the USS Essex (Sevenson 2014). The USS Essex is the U.S. Navy's amphibious assault ship.

Most ships go to sea duty for months at a time. Due to the remote location, it can be challenging for a massive navy vessel to pull into a town or go to a nearby place for spare parts. Using cargo helicopters might be the first option that comes to mind, but this is usually avoided due to high costs, plus excessive preparations are needed for helicopter's landing on the ship's helipad if the ship has one. The AM systems can provide stable and high-quality spare parts to support Marine and Army missions. Additive manufacturing has become an immediate option for manufacturing the needed parts offshore on navy vessels. However, the shipboard equipment suffers from a broad range of external excitations arising from the waves and the vessel's engines. That poses a concern for the quality of the 3D printed parts printed on shipboard. The main factor the quality of the 3D printed parts rest upon, besides layer thickness and the quality of the material used for 3D printing, is the vibration on the 3D printers. The manufacturing dimensions and tolerances can deviate from the acceptable values as a result of ship motion or shipboard

vibrations. As Severson et al. (2014) reported in their article, many military branches are calling for greater adoption of additive manufacturing, including the U.S. Navy. It is interesting to see how the printer performs; once the ship leaves the comfort of the dock, it is incredible to see a large cruise being tossed around due to powerful waves rocking the ship. Waves, and the vibration of the vessel's engines, which have a total output of 70,000 horsepower, could throw the calibration of the printers off (Severson 2014). It is known that the shipboard equipment is exposed to broadband vibration excitations (Mil-std 2005). Thus, the idea of 3D printing afloat brings questions about the viability of the process. No prior studies have been found for the vibration control systems of 3D printers on shipboard. In fact, on a recent solicitation, the U.S. Navy has called for innovative solutions to improve the quality of the 3D printed parts on navy vessels. Therefore, there is a pressing need for innovative ways to attenuate the external vibrations coming to the 3D printing equipment on shipboard.

Vibration isolation systems are used almost on every moving system that we see around. Examples include building structures, bridges, air-, land-, and sea-vehicles, smart phones, tablets, laptops, and many more. Vibration isolation systems can be categorized in four main groups: passive, active, hybrid, and semi-active (Hongnan Li and Huo 2010). Current passive mounts and isolators with (pre-set) damping characteristics used for vibration attenuation cannot support variable payload systems due to variation in the overall system dynamics (Kavlicoglu et al. 2020). The active systems are bulky, complex, and require high-power consumption and maintenance. The semi-active systems combine the advantages and eliminate the drawbacks of the passive and active suspension systems; they are less complex, more reliable, and require low power consumption (Swevers et al. 2007).

The magnetorheological (MR)-based isolation systems, a type of semi-active isolation systems, have been employed in various applications ranging from landing gear of aircraft to crashworthiness of helicopters, from prosthetic knees to weapon recoil, from automobile suspensions to off-road vehicles. A magnetorheological-based semi-active vibration isolator can offer both controllable damping and stiffness for precise vibration isolation. To this end, in this study, a novel semi-active vibration isolation system

called Magnetorheological-based Semi-Active Vibration Isolator (MR-SAVI for short) was proposed. MR-SAVI can operate at a wide range of frequencies and shift the AM equipment's natural frequency as needed. This thesis presents a comprehensive design methodology for a proof-of-concept MR-SAVI. The proposed design technique employs both analytical and simulation modeling, both of which are discussed in detail. The significant design parameters are identified and optimized via a comprehensive optimization program developed in Ansys. The generic method presented here can conveniently be used for future designs for different design requirements.

1.1 Hypothesis

It is hypothesized that proposed generic analytical and simulation modeling can be reasonably used for the design of MR-SAVI's.

1.2 Objectives

- Developing a design methodology for a novel smart vibration isolation system.
- Identifying the significant design parameters.
- Optimizing the significant design parameters based on the design requirements.

CHAPTER 2

LITERATURE REVIEW

2.1 Overview

The quality of the 3D printed parts can be affected by many factors, including printing material, layer thickness, printing speed, extrusion temperature, and so on. (Banjanin et al. 2018). While holding those factors constant, this paper aims to investigate the installation of a 3D printer on a shipboard with vibration isolators and its influences to improve the quality of the 3D printed parts. Because the manufacturing dimensions and tolerances could deviate significantly from the acceptable values as a result of waves, ship motion, and shipboard vibrations. A summary of research and development of active, passive, semi-active structural control devices and their roles for structural protection against wind, vibration, and seismic loads will be discussed in this chapter, including their capabilities and limitations, and followed by the use of magnetorheological technology; Magnetorheological Fluid (MRF) and Magnetorheological Elastomer (MRE), and the fabrication of MREs as one of the essential parts of this research.

2.2 Additive Manufacturing

Additive manufacturing (AM) has created a paradigm shift in manufacturing in the last two decades. This technological innovation, concocted during the 1980s, has gone global recently. It can deliver even the most complicated shapes, from micro- to macro-levels, at reduced weights and robust structural integrities. There are numerous applications of 3D printing, including medical, aerospace, energy, defense industries, which are likely to spread and revolutionize the whole industrial spectrum. Although the use of

3D printing is increasingly becoming common, more work still needs to be done to improve the quality of the printed parts.

Consequently, anchored on this reason, the constant basic, analytical modular examination ought to be conducted within the limits of the quality assessment (Rayna, Striukova, and Darlington 2015). Such systematic modular analyses assume exceptionally critical roles as far as evading potential disappointment. Figure 1 shows the workflow step by step in additive manufacturing. The first step is to create a 3D computer-aided design (CAD) model and converting the CAD model to STL format; the digital model is turned into a physical object by constructing the model layer at a time (Clark, Liska, and Mülhaupt 2017).

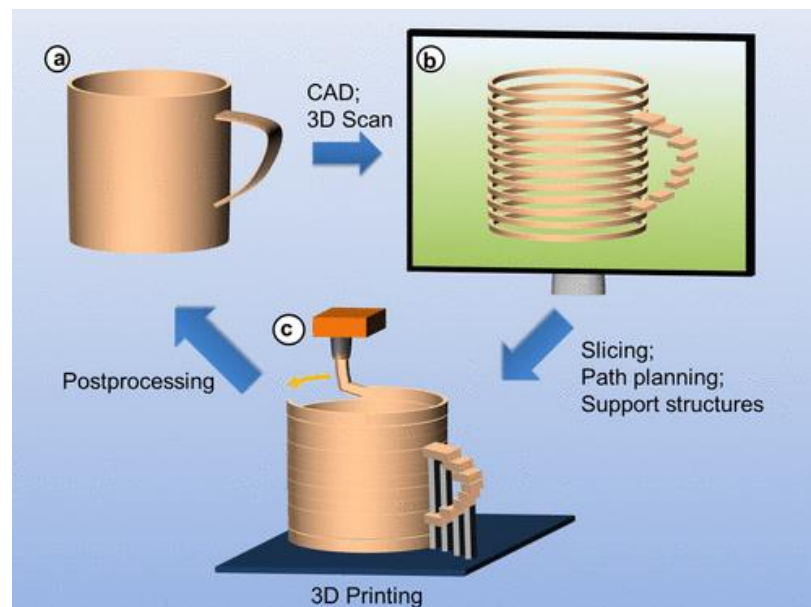


Figure 1: Overview of the typical additive manufacturing workflow: (a) turning an idea into a drawing using CAD, (b) preprocessing of model data, and (c) a digital model is turned into a physical object by adding material a layer at a time (Clark, Liska, and Mülhaupt 2017).

2.3 Structural Control System

Structural control systems can be grouped into four main categories: passive, active, hybrid, and semi-active control (Hongnan Li and Huo 2010). An active control system features an externally powered actuator mechanism to supply control forces to the structure, e.g., an active mass damper. On the other

hand, a passive control system is simple, reliable, and does not require an external power source, e.g., a tuned mass damper (Hongnan Li and Huo 2010). The use of active control systems and some combinations of passive and active systems are called hybrid systems (Soong and Spencer 2000). Semi-active control systems combine the best characteristics of both passive and active control systems. The semi-active control system is a class of active systems that only requires small external energy to tune the parameters of the control system, e.g., active variable damper (Hongnan Li and Huo 2010).

2.3.1 Active Isolation Systems

The active vibration isolation systems are bulky, complex, require high power consumption and high maintenance costs. However, they have the advantage that negative damping can be provided; a more extensive range of forces can be generated at low velocities, hence potentially improving system performance and adaptability to varying loading conditions (Swevers et al., 2007). Active control systems are composed of controllable force devices integrated with sensors, controllers, and real-time information processing (Soong and Spencer 2000). The sensor system measures the excitation input, such as acceleration to the structure. Then the control system acquires the input data from the sensors, computes the required counterforce, and sends a corresponding signal to the actuator system to produce the applied reaction force and offer a remarkable isolation performance (Cesmeci et al. 2019). Active control system research is very challenging, and it is indeed integrating several diverse disciplines. Starting from civil and mechanical engineering, including computer science, data processing, control theory, material science, sensing technology, structural dynamics, chemical, and wind and earthquake engineering (Soong and Spencer 2000).

2.3.2 Passive Isolation Systems

Passive isolation systems have a fixed (pre-set) damping characteristic, and they are not adaptable to varying loading conditions (Swevers et al., 2007). However, in the case of a power failure, the passive

components of the control still offer some degree of protection, unlike a fully active control system. Another advantage of using passive system techniques is that it provides a cost-effective means of protection. In other words, they are much simpler and more affordable and require low maintenance costs compared to the modern active systems.

Bridges are one of the applications that have been widely protected using passive isolation systems (Kunde and Jangid 2003). There are many cases of bridge collapses in the past due to wind loads. One of the most known case studies of engineering failure is the Tacoma Narrows Bridge in Tacoma, Washington. Bridges and skyscrapers are particularly vulnerable to damage and even collapse when subjected to wind loads, and to mitigate this wind-induced motion, that is when dampers become effective. The reliability of passive systems showed in Hayashikawa et al.'s (2000) investigation of the dynamic behavior of steel towers of the cable-stayed bridge subjected to significant three-dimensional earthquake ground motions. It is suggested the use of the passive control device and the seismic performance of steel towers with passive control device effectively reduce the reaction forces at the tower basements (Hayashikawa, Matsui, and Kaneko 2000). Along with the passive control system, there have been studies for semi-active control systems to better protect applications in both buildings and bridges.

2.3.3 Semi-Active Isolation Systems

Semi-active vibration isolation devices have received a great deal of research interest in the last two decades due to their being fail-safe, adaptive, and requiring less power usage. An additional benefit of the semi-active systems is that they require low fabrication and maintenance costs (Cesmeçi et al. 2019). Moreover, they have a fast response time, usually on the order of milliseconds (Ali and Ramaswamy 2009). Another attractive feature of a semi-active control system in case of a power outage is that the device would still operate in passive mode with some preset constant damping characteristics (Cesmeçi et al., 2019). Semi-active control systems were investigated in order to understand their performance through external excitations. Symans and Kelly (1998) investigated the effectiveness of semi-active dampers through an

analytical and computational study of a bridge's seismic response, which indicated that damage to the structure could be prevented or significantly reduced during an earthquake using semi-active dampers (Kunde and Jangid 2003). Control strategies based on semi-active devices integrate the best characteristic of both active and passive control systems (Soong and Spencer, 2000).

A semi-active damper system was installed back in 1998 in the Kajima Shizuoka Building in Japan. For the first time, a semi-active damper system applied to an actual building actively controls its response to severe earthquakes (Kobori, 2000; Kurata et al., 2004). As seen in Figure 2, the building's walls were equipped with semi-active dampers to empower it to be used as a disaster relief base in post-earthquake events (Kobori, 2000; Kurata et al., 2004). Each damper consists of a flow control valve, a check valve, and an accumulator and can develop a maximum damping force of 1,000 kN (Soong and Spencer, 2000). A sample of the response analysis results based on one of the selected control schemes and several earthquake input motions with the scaled maximum velocity of 50 cm/sec, together with a simulated Tokai wave, were illustrated in Figure 3 (Soong and Spencer, 2000). It was shown that both the story shear forces and drifts were significantly lowered when the control system was turned on. In the event of the shear forces, they are limited within their elastic-limit range while, without control, they would enter the plastic range (Kobori, 2000; Kurata et al., 2004). A semi-active control system can provide a large control force by changing parameters such as control device damping coefficient and stiffness; hence, it has the positive aspect that it can control the response of a large-scale structure in a severe earthquake with smaller energy when compared to the active systems utilizing an actuator, for example (Kurata 2004).

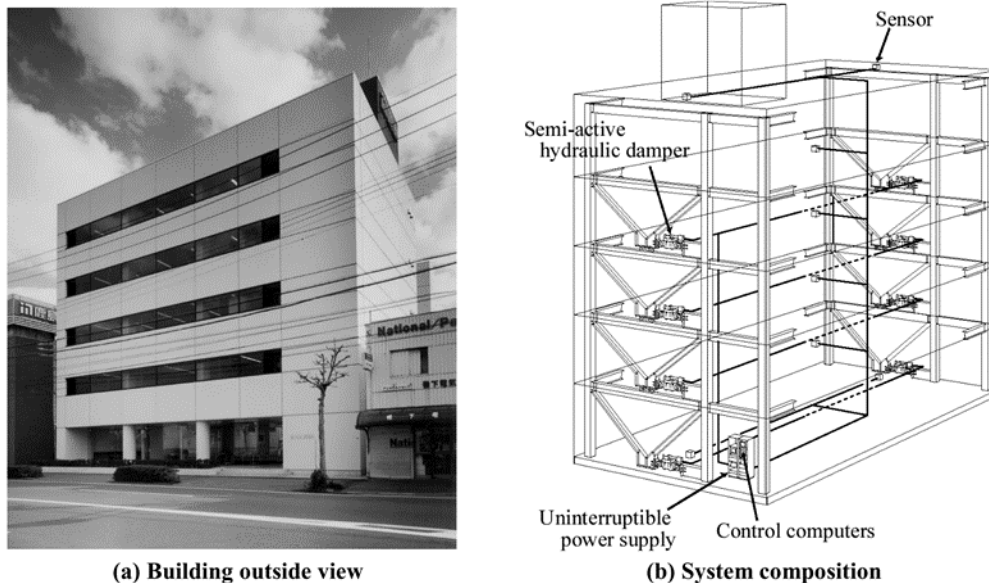


Figure 2: Kajima Shizuoka Building and Semi-active Hydraulic Damper (Kobori 2000).

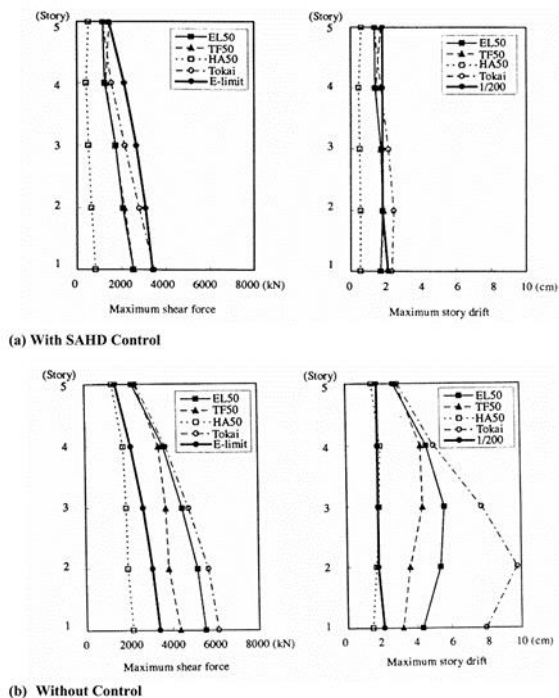


Figure 3: Maximum Responses (El Centro, Taft and Hachinohe Waves with 50 cm/sec and Assumed Tokai Waves) (Soong and Spencer 2000).

The semi-active damper, such as the MR damper, can generate the required damping force in a very short period of time, usually in less than a couple of hundred milliseconds, depending on the design and application (H. Li et al., 2012). The control sensors, typically the accelerometers, in the system read the external excitation input and transmit the signal to the control board. The control board then sends the required input signal to the electromagnet to tune the damping, and thus, the force applied by the damper (W. Eltahawy et al. 2018) as illustrated in (Figure 4). What makes the MR dampers even more desirable is their fail-safe feature. In the event of a power outage, during an earthquake, or an electronic failure, for example, the damper can still work as a passive oil damper with pre-designed damping properties.

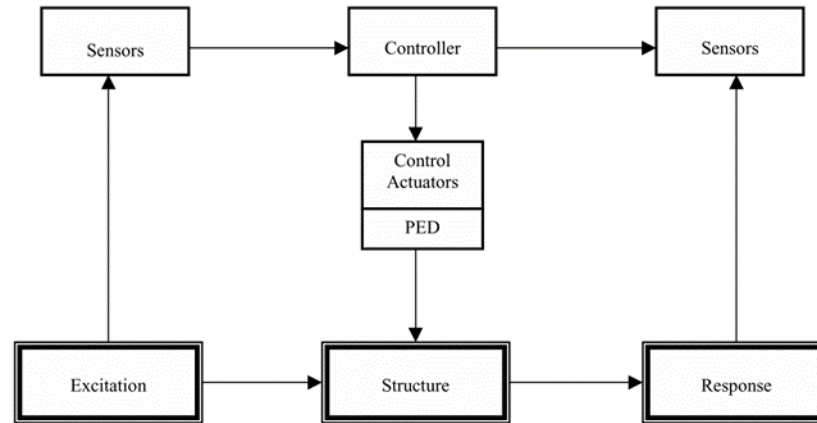


Figure 4: Structure with Semi-active Control (Soong and Spencer 2000).

2.4 Magnetorheological Vibration Isolators

MR damper is one type of the semi-active vibration isolator devices. They have been used for vibration attenuation in various applications, including civil engineering, automotive suspensions, aerospace, and navy sectors (Cesmeci et al. 2018). These devices employ a special kind of fluid – called MR fluid – from which the device takes its name. MR fluids are a kind of composite material consisting of micron-sized iron particles dispersed in a carrier fluid, usually hydrocarbon-based oils, which will be

elaborated on in the next section (Eltahawy et al. 2019). A typical MR damper houses a cylinder, piston, magnetic coil, and rod as well as the MR fluid, as shown in Figure 5.

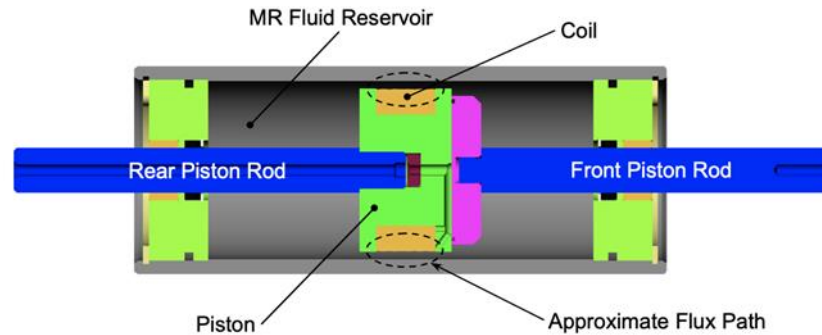


Figure 5: Typical MR damper components (Poynor and Reinholtz 2001).

2.4.1 Magnetorheological Fluid

MR materials, belonging to the functional smart material family, offer tunable rheological and viscoelastic characteristics such as shear stress, yield stress, dynamic modulus, and damping when exposed to an external applied magnetic field (Kwon, Lee, and Choi 2018). Traditionally there have been two major classes of MR materials: MR fluids and MR elastomers. The MR fluid is a smart fluid composed of micrometer-sized magnetic particles embedded in a carrier fluid such as silicon oil. They have the capability of changing their damping characteristics under applied magnetic fields (G. Li and Yang 2020). MR fluid transforms from viscous fluid to a solid-like paste with controllable yield stress in milliseconds when exposed to a magnetic field (Spaggiari 2012). The iron particles dispersed in the carrier fluid align in the direction of magnetic flux lines and form a chain-like structure, as shown in Figure 6. These chain-like structures restrain the fluid flow, thereby increasing the viscous characteristics of the suspension system (Delivorias 2004). By controlling the magnetic field's intensity, the shear strength of the MR fluid can be altered; hence, the resistance to flow can be varied. Activation and deactivation of the MR fluid can be done as soon as the magnetic field passes through the fluid and within milliseconds. When the magnetic field is removed, the chains are broken, and the iron particles return to their original distribution (Delivorias

2004). One of the positive aspects of MR fluid is that it is controllable and widely used for vibration control due to MR fluid's adjustable mechanical characteristics. MR fluid has many advantages, such as continuous tunable damping force, compact structure, long-term stability, low energy consumption, simple electronics, straightforward control, and fast response. MR fluids can be developed by mixing, for example, silicone oil with iron powder and adding some surfactants to retard the potential sedimentation in a laboratory environment. The MRFs are also commercially available and can be purchased from several vendors, including Lord Corporation, USA.

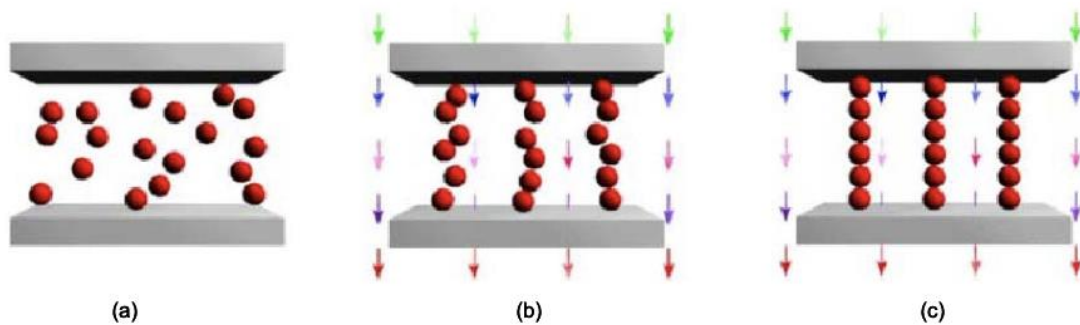


Figure 6: Activation of MR fluid: (a) no magnetic field applied; (b) magnetic field applied; (c) ferrous particle chains have formed (© 2005 Lord Corporation All rights reserved).

2.4.2 Magnetorheological Elastomer

Magnetorheological elastomers (MREs) have received considerable attention in recent years. An MRE, belonging to the MR material family, is a type of composite material with magnetic particles embedded in a non-magnetic elastomeric matrix. MREs can operate in a wide range of frequencies, tolerate large shear deformations, and have a speedy response time of a couple of milliseconds (Behrooz, Wang, and Gordaninejad 2014). When exposed to an external magnetic field, the stiffness of the MREs alters such that as the magnetic field increases, the stiffness increases. As a result, the MRE provides a controllable stiffness that can conveniently be used to shift the resonant frequencies of structures. When the magnetic field is removed, the material retrieves its initial property (Y. Li et al. 2014). MREs also have inherent

damping along with their stiffness features. MREs possess very similar advantages to those of MRFs. However, MREs can eliminate some disadvantages, such as the settling of magnetic particles that frequently occurs in MRFs. MREs do not have any fluid leakage problems, and thus, they don't require any sealing components (Dong et al., 2009).

2.4.2.1 Magnetorheological Elastomer Fabrication

There are two categories of MREs. They are distinguished by the distribution of magnetic particles within the elastomer: isotropic and anisotropic MREs. The fabrication process of MREs consists of three steps: mixing, degassing, and curing with magnetic particle orientation, as illustrated in Figure 7 (Kwon, Lee, and Choi 2018). First, all ingredients, including magnetic particles, elastomeric matrix, and additives, are mixed under a sufficient processing temperature to remove air bubbles inside the mixture. The air entrapped in the MRE mixture can alternatively be removed by putting the mixture in a vacuum chamber. Next, the isotropic MR elastomers are cured without the presence of a magnetic field. In contrast, the anisotropic MR elastomers are cured with the presence of a magnetic field (Kwon, Lee, and Choi 2018).

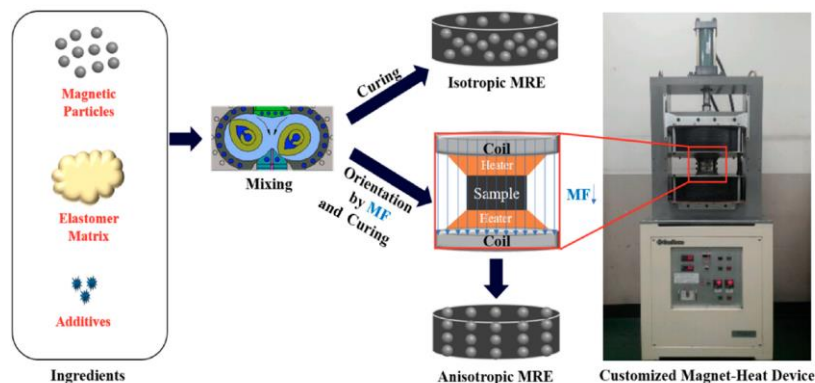


Figure 7: Schematic diagram of fabrication process of isotropic and anisotropic MREs (Kwon, Lee, and Choi 2018).

The curing process for anisotropic materials requires a strong magnetic field above 0.8 T to form chain-like structures of magnetic particles in the matrix. A constant temperature is also required to maintain the

flexibility of the magnetic particles for both isotropic and anisotropic materials during curing (Y. Li et al., 2014). The temperature varies depending on the elastomer matrix; some require only a room temperature, and others require a temperature above 120 °C. After the curing process, the magnetic particles are locked in the matrix, and only extra work can force the particles to move away from their original positions. Following the curing process, the cured sample is subjected to a further chemical process called vulcanization. The process is to modify the polymer by forming cross-links between the individual polymer chains, thus creating a more durable material (Y. Li et al., 2014).

Isotropic MRE's magnetic particles are homogeneously distributed. In an anisotropic MR elastomer, magnetic particles are distributed in the elastomer in a particular pattern that might offer a higher MR effect (Bastola, Paudel, and Li 2018). Isotropic MREs are relatively easy to make by simply mixing iron particles with silicone oil and silicon rubber, then pouring the mixture into a mold and degassed in a vacuum (Kallio et al., 2007). When the MRE samples were subjected to an external magnetic field during curing, the iron particles form a chain-like structure, forming an anisotropic MRE.

Fabrication of anisotropic MRE samples can be complicated due to the magnetic particles' particular arrangement in the elastomer, which can be done with several different methods. One of the best ways to fabricate an anisotropic MRE sample is to use a 3D printer, which allows the creation of MREs with completely arbitrary distributions of magnetic particles within the matrix material (Vaezi and Yang 2014).

Bastola et al. (2018) fabricated MRE illustrated in Figure 8 using a 3D printer with a multi-material printing technique. Each layer required a series of steps. The printer has multiple heads, one filled with MRF and the other with the elastomer matrix resin, and it was equipped with a UV unit, which was used for curing (Bastola, Paudel, and Li 2018). As illustrated in Figure 25, the elastomer matrix resin was dispensed from the nozzle forming a bottom layer, and then it was cured with UV light. After that, on top of the bottom layer, various structures of MRF filaments were printed from another nozzle. After that, those printed patterns were covered entirely by the elastomer matrix resin from the previous nozzle, and then it

was fully cured with UV light (Bastola, Paudel, and Li 2018). In this way, the first layer of MRE was completed. The process was repeated until the desired thickness of the sample was achieved.

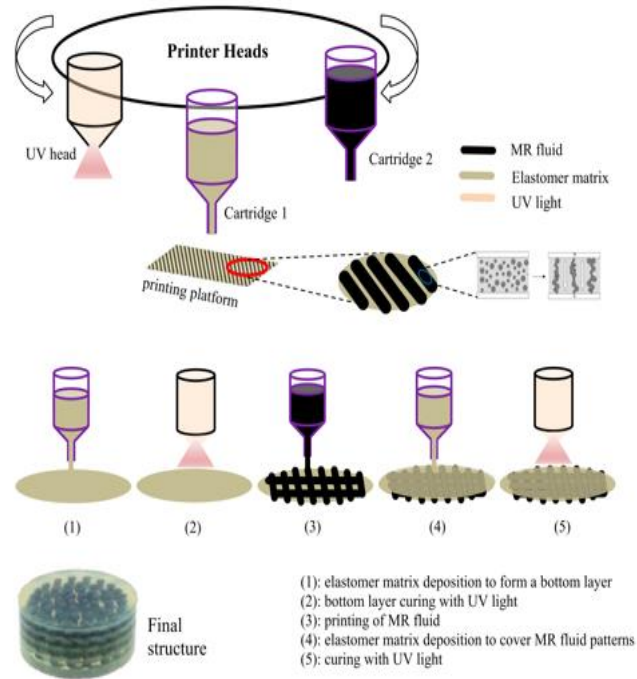


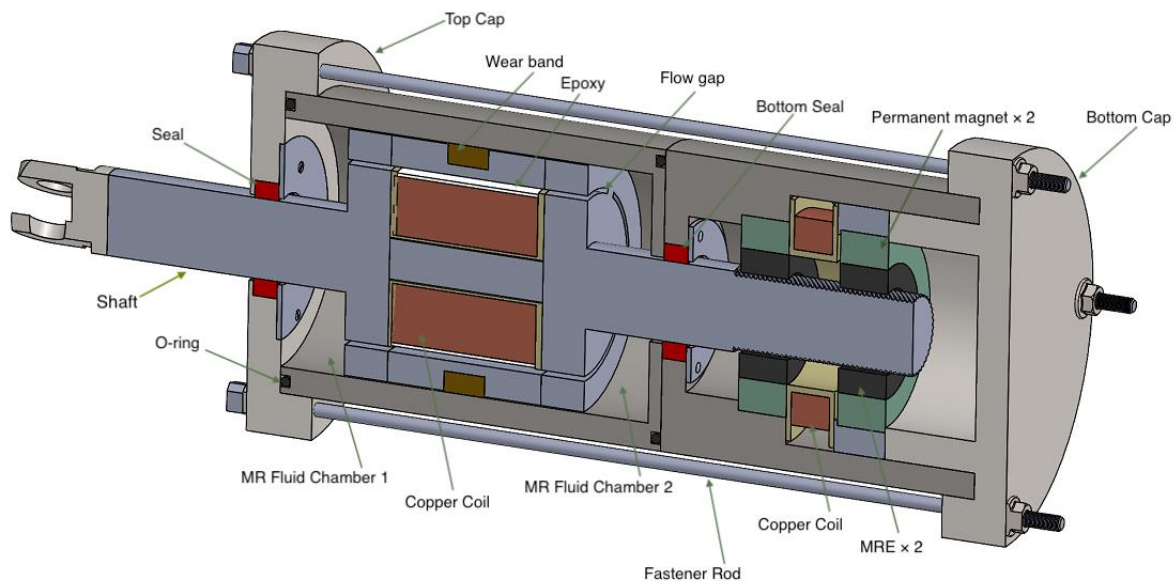
Figure 8: Schematic illustration for printing of hybrid MRE via extrusion printing (Bastola, Paudel, and Li 2018).

CHAPTER 3

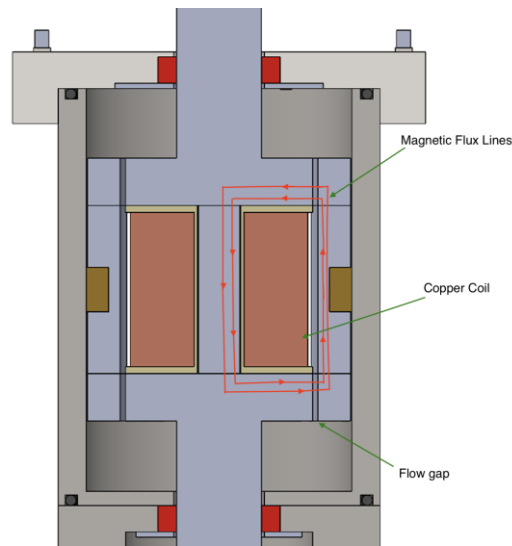
METHODOLOGY

3.1 Overview

The Magnetorheological-based Semi-Active Vibration Isolator (MR-SAVI) employs both the MRF and MRE technologies. The top part contains MRF-132DG enclosed in a cylinder with two chambers and a moving piston with a shaft. The bottom part houses two MREs, working in shear mode, two permanent magnets, and an electromagnet. Top and bottom caps close the ends of the cylinder, and four external rods fasten the caps against the cylinder, as shown in Figure 9 (a). A wear band between the piston and the inner wall of the cylinder helps to keep the piston centered, allowing for even pressure distributions on the seals. In addition, the piston features an annular flow gap, where the MRF is passing through when the shaft is reciprocating.



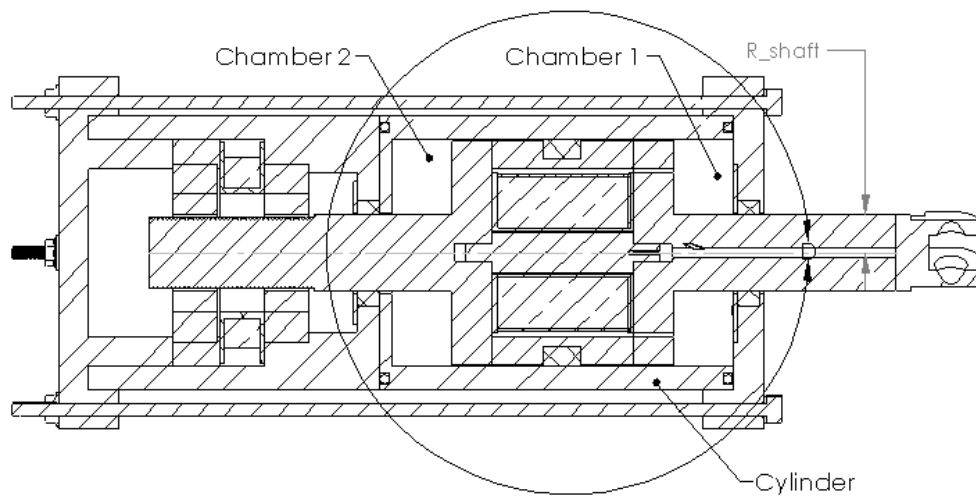
(a)



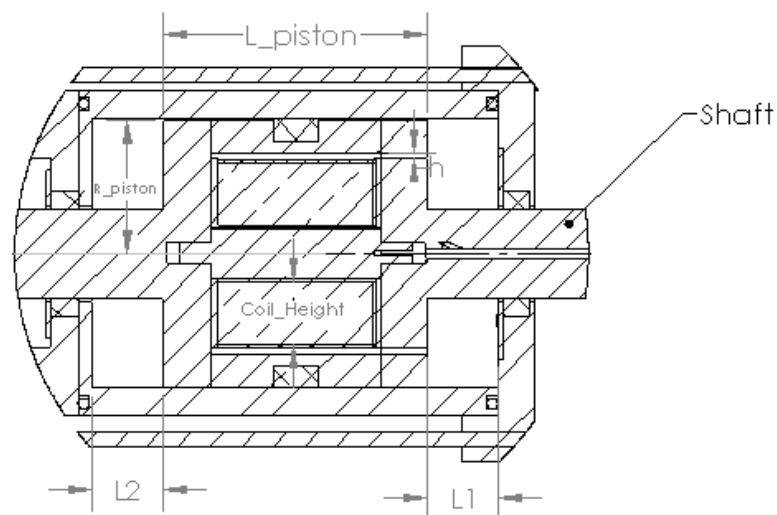
(b)

Figure 9: (a) Isometric cross-section view of the MR-SAVI and (b) detailed view demonstrating the generated magnetic flux lines in the flow gap.

The piston splits the top part into chamber 1 and 2. As the piston moves toward the bottom, the annular flow gap allows the MR fluid to flow from chamber 2 to chamber 1. However, during the rebound phase, the piston rod tries to restore its position against the compressive energy. As a result, the previously displaced fluid in the top chamber is pulled back through the annular gap to chamber 2. The piston also houses a copper coil to create a variable magnetic field to control the flow of MRF through the flow gap. When the coil is energized, an electromagnetic field is developed in the flow gap, which activates the MR fluid and generates a controllable MR damping in addition to passive viscous damping Figure 9 (b). Furthermore, there will be an additional contribution to the damping by the MRE changing the equivalent damping of the whole system.



(a)



(b)

Figure 10: The significant geometric design parameters. (a) 2D cross-section view of the MR-SAVI (b) detail view of the top part of the device where it carries the MR fluid.

In general product development, one of the initial processes is identifying the system or design requirements. Literature suggests that the design requirements for MR devices generally include the scale of the prototype, weight of the structure, design stroke, design frequency, design passive stiffness, design

passive damping ratio, and dynamic range. The power consumption and geometric (or space) constraints can also be added to this list as these can also be optimized along with the parameters listed. The design requirements for MR-SAVI are given in Table 1.

Table 1: Design requirements for MR-SAVI

The scale of the prototype	S
Weight of the structure (including the variable weight of the 3D printed part)	W
Design stroke	X
Design frequency	f
Design passive equivalent stiffness	k
Design passive equivalent damping ratio	ζ
Dynamic range	D
Maximum power	P

The focus of this study is to develop a design methodology for a proof-of-concept MR-SAVI. Hence, only the representative values of some of the design parameters are considered; frequency $f = 4$ Hz, the stroke, $X = 0.635$ cm, viscous damping ratio $\zeta = 0.2$, and dynamic range, $D = 2.5$. These values are determined based on literature and experience, considering both the time and resource constraints.

The design of the MR-SAVI includes both analytical and simulation modeling. The proposed analytical model identifies and superimposes all the force components due to both MRF and MRE parts. These forces include the seal friction force, spring force due to MREs, viscous damping force due to MREs, controllable MR damping force due to MREs, viscous damping force due to MRF, and controllable damping force due to MRF. There is currently no analytical modeling available in the literature for the MREs. Previous designs followed the following design procedure: first, the MREs were fabricated, then tested to obtain the force vs. displacement characterization curves. Next, the proposed phenomenological models were utilized to describe the dynamic behavior of the MREs. These models incorporated

coefficients that are functions of stroke, frequency, and current. These coefficients were identified based on the experimental data and used for the design of future MREs. Basically, the output force of the MREs could be predicted based on the stroke, frequency, and current information, which could be used at the design stages for the next MREs. However, the fabrication and characterization of the MREs are beyond the scope of this work. This study rather outlines the design methodology of the MR-SAVI and focuses on the design of the MRF component. The reader should be reminded that the design of MR-SAVI is a very involved task, and the focus on the MRF component only is deemed to be sophisticated enough to occupy this thesis.

The proposed analytical modeling for the MR-SAVI involves parameters that are functions of magnetic field developed in the flow gap. The magnetic field information could be readily obtained via theoretical electromagnetic analyses, however, at the expense of loss in accuracy. A reasonable alternative is computer simulations. Also, the parameters in the analytical model are related to each other. For example, while the flow gap, h , increases, the dynamic range, D , increases, but the viscous damping ratio, ζ , decreases. Furthermore, the temperature has been known to affect the performance of MR devices, which should be accounted for at the design stage (Cesmeci et al. 2010). Electromagnetic analysis and thermal analyses can be conveniently conducted on a Finite Element Analysis (FEA) software (Sahin, Cesmeci, and Wereley 2011). Thus, an optimal design method would be integrating the software results with the analytical formulations. Ansys is a good candidate to do such a task. While the electromagnetic and thermal simulations could be performed on Maxwell and Heat Transfer modules, an Excel module could be used to carry out the analytical calculations. Therefore, a comprehensive program is developed in Ansys platform to carry out the simulations and analytical calculations simultaneously, followed by an optimization study on the same platform.

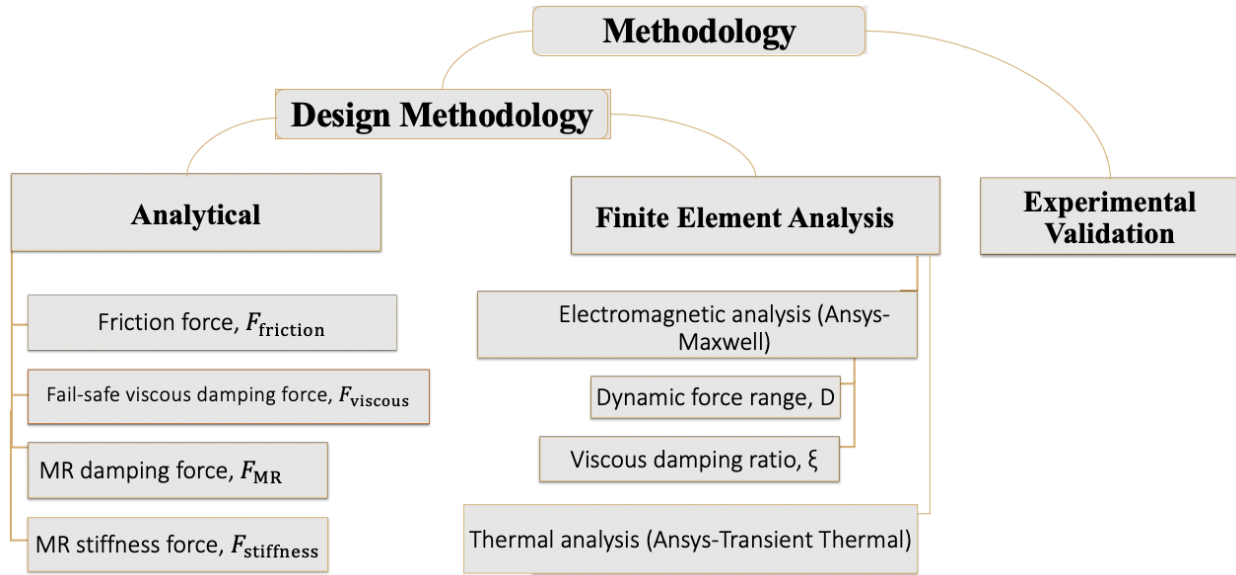


Figure 11: The schematic diagram for the Design Methodology of MR-SAVI.

The critical geometric design parameters used in analytical and finite element modeling are shown in Figure 10.

3.2 Analytical Modeling

The analytical modeling of the MR devices starts with dynamic range discussions. Dynamic range, D , is a measure of the performance of an MR damper (Cesmeci 2017). It is described as the ratio of the total damper force to the uncontrollable damping forces and can be expressed in math (Yang et. a. 2002):

$$D = \frac{F_{damper}}{F_{uncontrollable}} = \frac{F_{MR} + F_{viscous} + F_{seal}}{F_{viscous} + F_{seal}} = 1 + \frac{F_{MR}}{F_{viscous} + F_{seal}} \quad (3.1)$$

The combination of forces produced by different parts of MR-SAVI will be discussed in this section. For MR-SAVI, the total device force is the combination of seal friction, spring, viscous damping, and MR damping forces.

$$F_{device} = F_{seal} + F_{spring,MRE} + F_{viscous,MRF} + F_{MR,MRF} + F_{viscous,MRF} + F_{MR,MRF} \quad (3.2)$$

The fail-safe MRF viscous damping and controllable MR damping forces are discussed in subsections 3.2.1 and 3.2.2, respectively. Seal force and Spring force are representative force values to assist the current study, and these values are based on literature review and experience within an acceptable range. Spring force is coming from MRE.

3.2.1 Viscous Damping Force

The device acts as a passive damper when there is no electromagnetic field applied. As the piston moves toward the base, the MR fluid flows to chamber 1 from chamber 2 through the annular flow gap within the piston, thereby generating a viscous dissipation. The force generated due to the viscous flow through the flow gap is well established and is given by (Yang et al. 2002).

$$F_{viscous} = \left(1 + \frac{w h V_p}{2 Q}\right) \frac{12 \mu Q L_{piston} A_p}{w h^3} \quad (3.3)$$

where,

A_p : The effective piston area

w : The mean circumference of the flow path

V_p : The piston velocity

μ : The plastic viscosity of the MR fluid

Q : The flow rate through the gap

L_{piston} : The axial length of the piston

h : The height of the gap

3.2.2 MR Damping Force

Controllable MR dampers dynamically change their properties to accommodate varying loading conditions (Li and Huo 2010). They do this by utilizing the unique properties of the MRFs. MRFs behave as a typical Newtonian fluid under no magnetic field. However, under the influence of an external magnetic field, MRFs change their state from liquid to semi-solid. In this state, to initiate a flow, a certain pre-stress must be applied to the fluid. This unique behavior renders MRF to be a non-Newtonian fluid. This type of fluid behavior can be represented conveniently with the simple Bingham plastic model (Cesmeci 2017). Graphical representation of the Bingham plastic model is shown in Figure 12.

$$\tau = \tau_y + \mu \dot{\gamma} \quad \tau > \tau_y \quad (3.4)$$

τ = The shear stress

τ_y = The yield stress

μ = The plastic viscosity

$\dot{\gamma}$ = The shear strain rate

τ_y is a function of the magnetic field and can be controlled with the intensity of the applied magnetic field.

The Bingham plastic model is also represented in Figure 12.

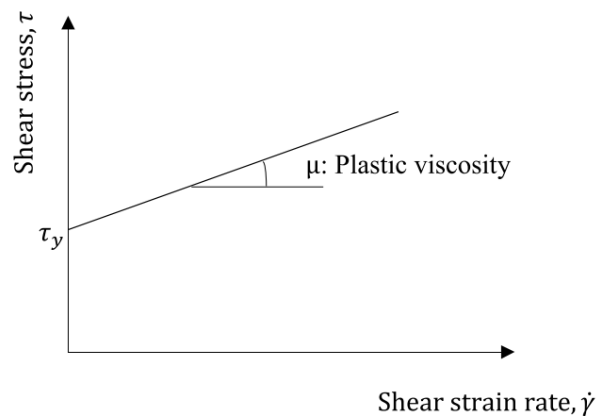


Figure 12 : Graphical representation of the Bingham plastic model (Cesmeci 2017)

The controllable MR force based on the parallel plate approximation and Bingham plastic model by Yang et al. (2002):

$$F_{MR} = \left(2.07 + \frac{12 Q \mu}{12 Q \mu + 0.4 w h^2 \tau_y(B)}\right) \frac{\tau_y(B) L A_p}{h} \text{sgn}(V_p) \quad (3.5)$$

A_p : The effective piston area

w : The mean circumference of the annular flow gap

Sgn: signum function

V_p : The piston velocity

μ : The plastic viscosity of the MR fluid

Q : The flowrate through the annular gap

L_{piston} : The axial length of the piston

h : The height of the gap

L : The effective axial pole length "active pole"

3.3 Finite Element Modeling

The design of MR-SAVI involves finite element modeling in addition to the theoretical modeling discussed in Section 3.2. This section discusses an optimization study that determines the optimal geometric parameters, incorporating electromagnetic and thermal analyses. The model geometries here are drawn based on the optimized geometric parameters listed in Section 4.3.

Computer simulations can be effectively used to assist such study, better understand and optimize the system performance to demonstrate its reliability. For example, to calculate the dynamic range, the yield stress of the MRF in the flow gap has to be known. This could be done using 1D Maxwell's equations; however, more accurate information of the yield stress can be obtained by running 3D electromagnetic

FEA, using commercially available software packages such as Ansys Maxwell. Also, Microsoft Excel Module in Ansys can be used to host and employ the theoretical equations that will be used as a part of the proposed design methodology. These two modules, along with others such as Ansys Geometry module, can be integrated to develop a comprehensive optimization program in Ansys platform to seek the optimal design parameters for the MR-SAVI.

3.3.1 Electromagnetic Analysis

Currents passing through coil wires generate a magnetic field. When the MR is exposed to a magnetic field while passing through the MR valve, the damper acts in the semi-active mode, increasing the fluid's viscosity, supplying additional damping that varies with the intensity of the magnetic field. This is what could be termed "controllable MR damping force," which also involves calculating the dynamic yield stress, $\tau(B)$, of the MR fluid. For the purpose of obtaining $\tau(B)$, the magnetic flux density, B , developed in the flow gap needs to be known (Cesmeci 2017). The magnetic flux density, B , can be estimated using finite element analysis (FEA). In this study, ANSYS Maxwell module is used to calculate the B in the flow gap. The 3D model is designed, and analyses are conducted. The analyses are applied to the entire device model. However, the magnetic field concentrations are around the piston area, including the MREs and permanent magnets in the bottom part of the device.

The Geometry Module in ANSYS is used to create a 3D model geometry. Next, the geometry file is imported into the Maxwell Module, and related materials are assigned to each component. Low-Carbon Steel Grade AISI 1018 is selected for the shaft, cylinder, top, and bottom caps. MRF 132-DG is assigned to the MR fluid in the chambers. MRE material to the MRE samples, and NdFeB 35 is assigned to permanent magnets. Copper material is assigned to the coils.

AISI 1010 with proper magnetic properties is chosen for the shaft and the cylinder to help to develop the magnetic field in the targeted areas. The relationship between the magnetic flux density, B , and

magnetic field intensity, H ; the yield stress, τ , and magnetic field intensity, H , for the fluid is given by the following expressions (© 2005 Lord Corporation).

$$B = 0.68[1 - e^{(-10.97\mu_0 H)}] + \mu_0 H \quad (3.6)$$

$$\tau = 63,855.60 \tanh(6.33 \times 10^{-6} H) \quad (3.7)$$

Where B is in Tesla, H is in A/m, τ is in Pa, and $\mu_0 = 4\pi \times 10^{-7} \text{ T/(A/m)}$ is the magnetic constant (Cesmeci 2017).

3.3.2 Thermal Analysis

As in the case of the electromagnetic analyses discussed earlier, theoretical formulations, such as lumped parameter method, can be used to calculate a 1D temperature profile to address the effects of heating on the performance of the MR-SAVI. However, again, FEA offers a more convenient way to obtain 2D or 3D and more accurate results for the temperature field on the device. To this end, the Transient Thermal module is used to carry out the transient heat transfer simulations in Ansys. The total energy dissipation from the device can be calculated from the area under a force vs. displacement loop (Cesmeci 2017). This energy becomes a heat source to the MR fluid, which eventually increases the fluid temperature and affects the device's performance. The device components are subject to failure due to overheating, and that includes seals. Heat damage leads to reduced seal life. McKee et al. demonstrated the effects of temperature on the performance of seals (McKee, Gordaninejad, and Wang 2018). They reported that increased temperature expanded the seals, resulting in deformation on the seals, which shortened the seal life. Moreover, the expansion on the seals caused an increase in the friction force because the seal lips pushed stronger against the shaft before the failure occurred. Furthermore, according to Curie's law, as the temperature increases, the iron particles inside the MR fluid partially lose their ability to be magnetized; therefore, magnetization decreases.

The copper coils in the MR-SAVI generate electromagnetic heating; additional heating energy sources in the device when the coils are energized. Although copper has high electrical conductivity, there is some resistance to electrical current, causing Ohmic power losses, which transforms into heating (Cesmeci 2017). When the energy of an electric current is converted into heat through the electrical resistance, the Joule heating raises the temperature in coils and surroundings. As the temperature in the coils increases, the resistance of the wires increases (Cesmeci 2017). So, this requires additional power for the coils to maintain the same magnetic field in the MR fluid. The heat transfer to the piston and cylinder wall from both the MR fluid and coils consequently reduces the efficiency of the electromagnet. All these concerns should be taken into consideration in the design of MR-SAVI.

Thermal analysis is performed using the Transient Thermal module in ANSYS. The thermal analysis involves theoretical calculations to determine the heat generation due to viscous dissipation and an electromagnetic analysis to calculate the heat generation from Joule heating. All theoretical calculations are performed in the Excel module, whereas the Maxwell module performs the electromagnetic analysis. The calculated heat sources are linked to the Transient Thermal module. Figure 13 shows the schematic of a comprehensive multi-objective optimization developed in ANSYS platform where Electromagnetic, Transient Thermal Heating, and Microsoft Excel modules are integrated to determine the optimal geometry of the device.

An Excel spreadsheet module is programmed to do all calculations, including the total viscous heating. The Excel module passes the viscous heating value as heat input to the Transient Thermal module. The calculation of the MR damping force requires information about the magnetic flux density in the flow gap. This information is transferred to the Excel module from the Maxwell module. On the other hand, the Joule heating is calculated by the Maxwell module directly. The Joule heating (*aka* Ohmic losses) data from Maxwell 3D is transferred to ANSYS Transient Thermal to observe the temperature rise over time. This is verified with the formulation for the Joule heating, $Q = I^2R$, where I is the current and R is the resistance of the coil. The device is to be cooled with a fan at room temperature during the tests. The forced convection,

a convection boundary condition with $T = 22\text{ }^{\circ}\text{C}$ room temperature and $h = 50\text{ W/m}^2\cdot^{\circ}\text{C}$, is considered and assigned to all outer surfaces of the device based on literature (Cesmeci 2017). The total viscous heating is calculated by the superposition of the seal friction, viscous, and MR damping as,

$$W_{Total} = 2 F_{friction} + \pi F_{viscous} X + 4 F_{MR} X \quad (3.8)$$

CHAPTER 4

RESULTS AND DISCUSSION

4.1 Electromagnetic Analysis Results

The results for magnetic flux density, B , in the flow gap for the current input of 1000 A x turns are shown in Figure 13. These results are from the electromagnetic analysis discussed earlier. The regions in the flow channel where the magnetic field is developed are called active pole regions. Whereas the region next to the coil is called the passive pole length since there is no magnetic field generated in that region. These regions are labeled in Figure 13 a.

In order to achieve a higher Dynamic range, D , F_{MR} must be maximized while $F_{viscous}$ is minimized, and F_{seal} is usually constant within a reasonable range as illustrated by Eq. (2.1) (Cesmeci 2017).

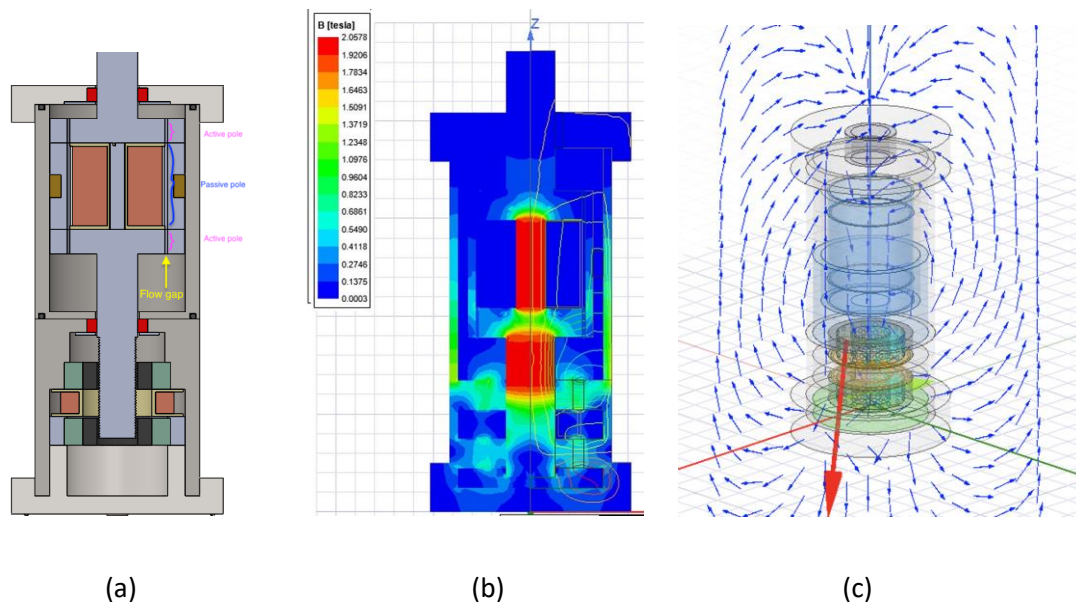
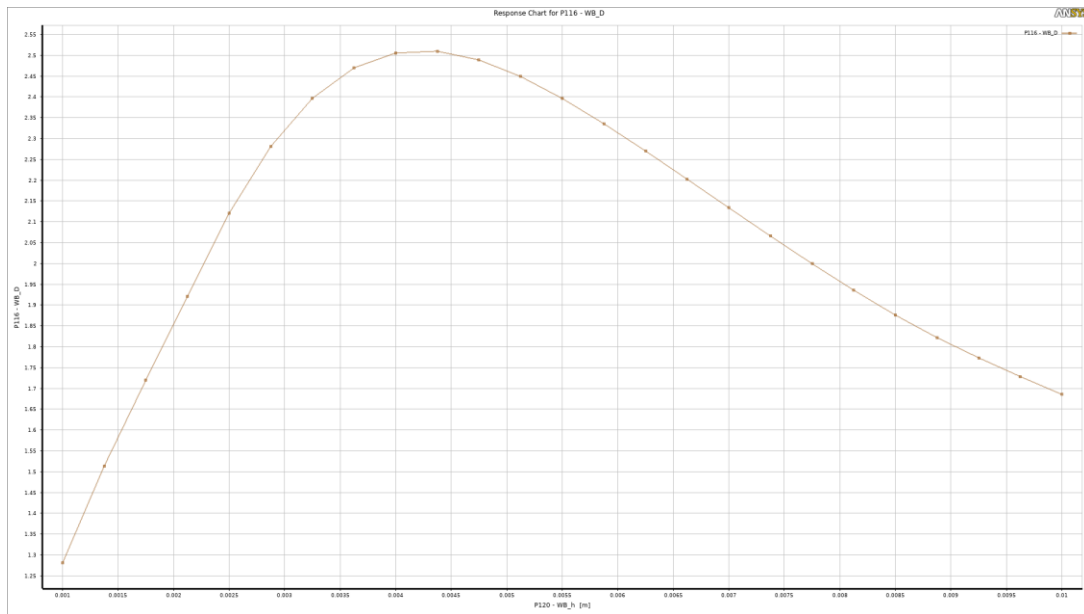


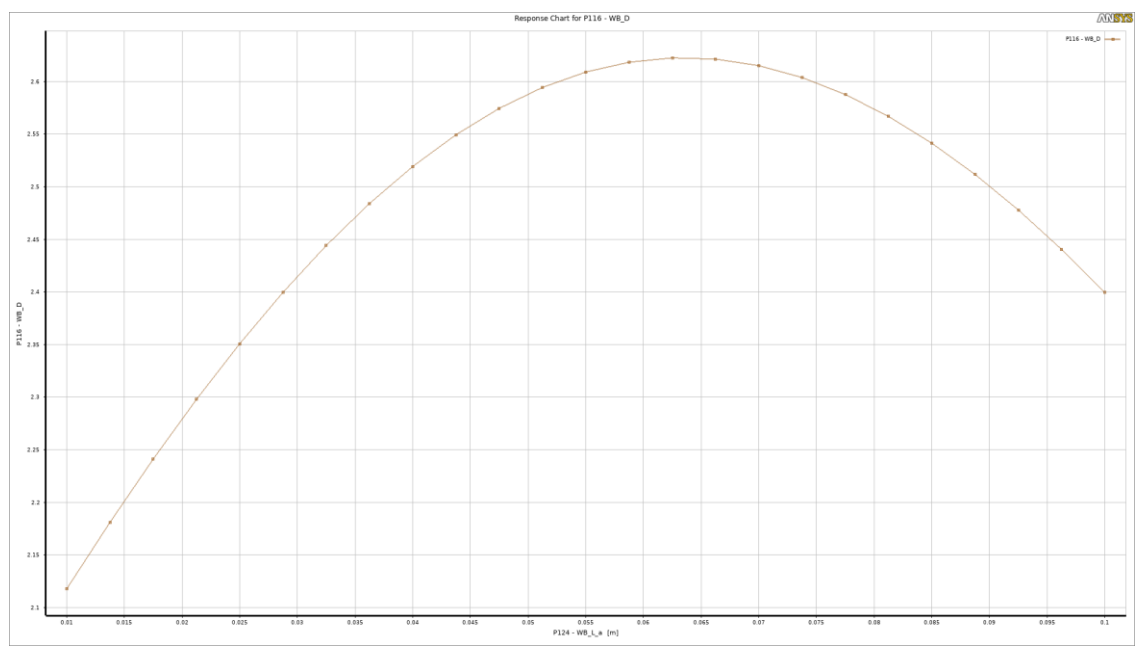
Figure 13: (a) CAD model cross section view of MR-SAVI (b) magnetic flux density distribution B magnitude using Maxwell 2D, (c) B vector using Maxwell 3D vector in electromagnetic analysis with current input of 1000 A x turns.

F_{MR} and $F_{viscous}$ are both functions of the height of the flow gap, h , active pole and length, L_a . It is observed that increasing the value of the height of the flow gap, h , decreases the F_{MR} and $F_{viscous}$, which results in reducing the value of the dynamic range, D , presented in Figure 14 a.

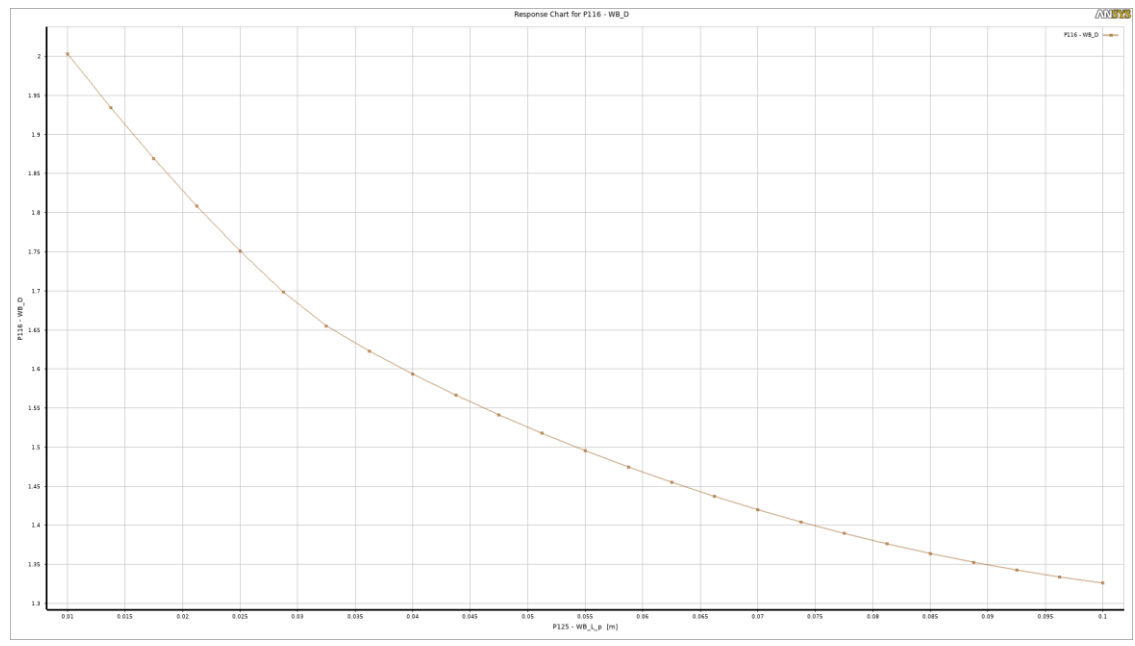
Furthermore, the response surface of L_a shows that increasing the active pole length, L_a , increases F_{MR} and thus, increases D . It is important to point out that increasing L_a increases the magnetic field generated in the flow gap, which provides high dynamic yield stress, $\tau(B)$, and eventually increases F_{MR} as $\tau(B)$, is a multiplier in F_{MR} . Considering the magnetic saturation of the MR fluid, the $\tau(B)$, is limited by the magnetic field saturation. F_{MR} increases with increasing L_a since L_a is a multiplier in F_{MR} equation. Considering the above-mentioned, L_a increases the axial length of the piston. Thus, it increases L_{piston} , resulting in decreasing D . The variations of D with h , L_a , L_p are illustrated in Figure 14.



(a)



(b)



(c)

Figure 14: Variation of dynamic force range, D, with respect to the (a) flow gap, (b) active pole length, (c) passive pole length.

Another important design requirement is the viscous damping ratio, which is also a function of geometric dimensions of the MR valve as well as fluid properties:

$$\zeta_{viscous} = \left(\frac{W}{\pi \omega_d X^2} \right) \left(\frac{1}{2\sqrt{KM}} \right) \quad (4.1)$$

ω_d : The driving frequency

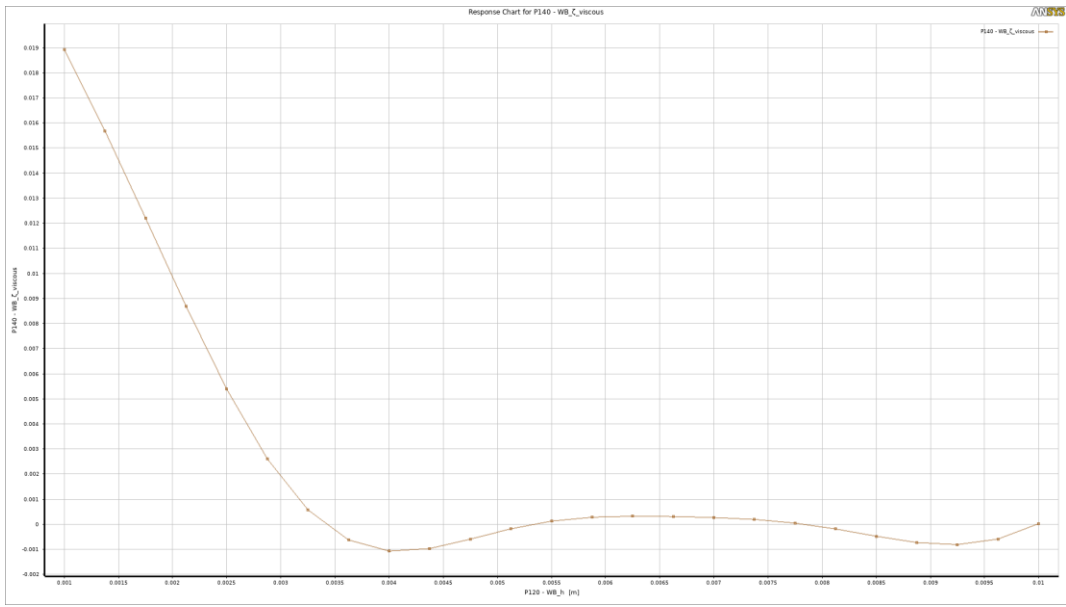
M : The mass

K : Spring constant

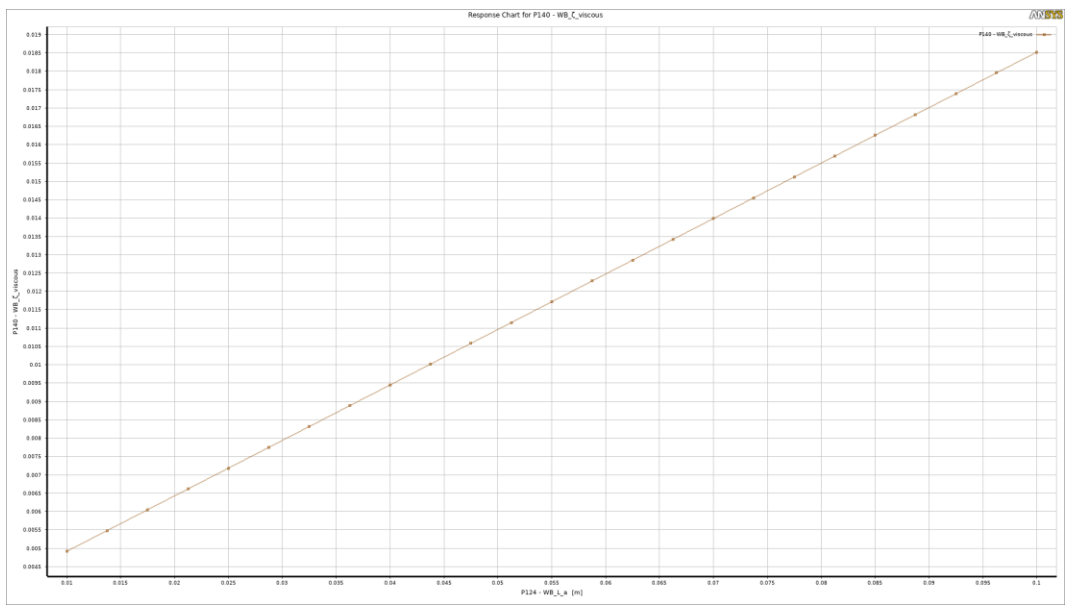
X : Amplitude of the harmonic excitation

where $W = \int_0^{2\pi/\omega_d} F_{viscous}$ is the energy dissipation due to viscous dissipation.

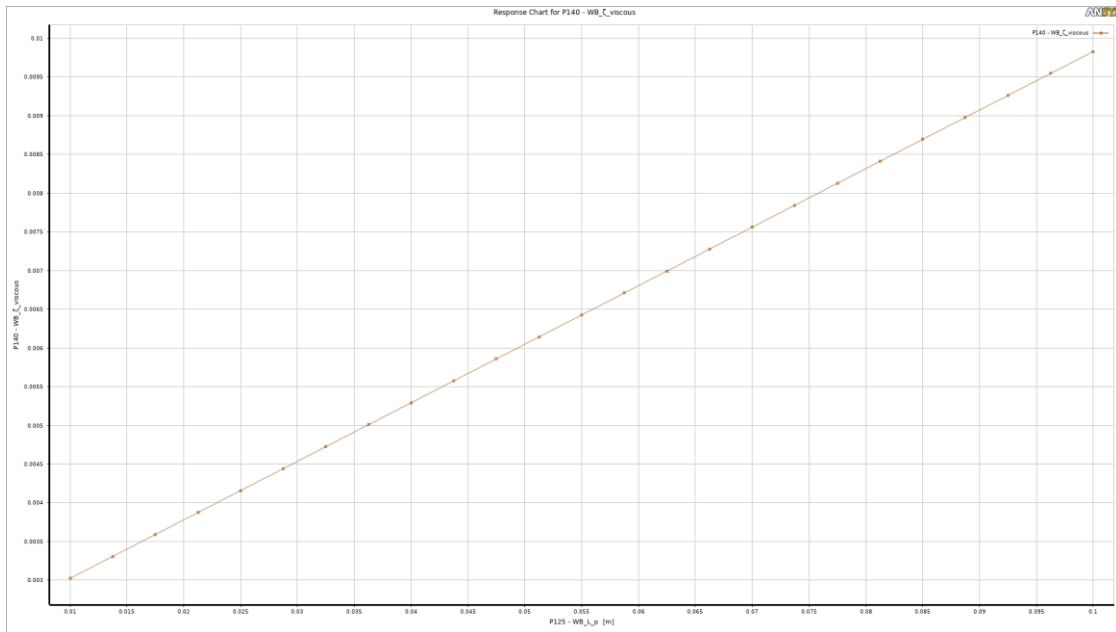
There are several ways in which the viscous damping ratio, ζ , can be affected by h , L_a , or L_p . The value of the viscous damping ratio, ζ , significantly decreases with increasing values of the flow gap, h , as $F_{viscous}$ is inversely proportional to the h in equation (3.3) as shown in Figure 15 a. Conversely, $\zeta_{viscous}$ increases linearly with increasing L_a , and L_p as the two parameters increase the axial length of the piston, L_{piston} , which is a multiplier in $F_{viscous}$ (equation 3.3). The effects of L_a , and L_p on $F_{viscous}$ are illustrated in Figure 15 b, Figure 15 c. Therefore, there must be an optimal value for h , L_a , and L_p to reach the given target for $\zeta_{viscous}$. The procedures to obtain the optimal values of these parameters are discussed in Section 4.3.



(a)



(b)



(c)

Figure 15: Variation of of viscous damping ratio, $\zeta_{viscous}$, with respect to the (a) flow gap, (b) active pole length, (c) passive pole length.

4.2 Thermal Analysis Results

The temperature distribution in the device was obtained from the Transient Thermal heating analysis. The accuracy of the thermal analysis is highly dependent on the boundary conditions. The boundary condition for the transient thermal analysis is set to be forced convection, *i.e.*, a convection boundary condition with $T = 22$ °C room temperature and $h = 50$ W/m²°C. The device temperature remained stable, with negligible increment. This is mainly because the thermal simulations are carried out only for 4 complete cycles as well as the low force levels of the device. Again, this simulation time was only a representative time. For an actual application, depending on the type of printer and part that is going to be printed, the maximum operating time of the MR-SAVI should be estimated, and the heat transfer analyses should be run accordingly to account for the deteriorating effects of temperature on the performance of the MR-SAVI. The concentration of temperature is found to be in the MRF area in chambers 1 and 2. There is

no heat transfer from the inner surface of the chambers to the outside wall of the cylinders as shown in Figure 166. The temperature distribution in the MR fluid for $X = 0.00635$ m, $t = 0.25$ to 1 sec, and $I = 1000$ A x turns.

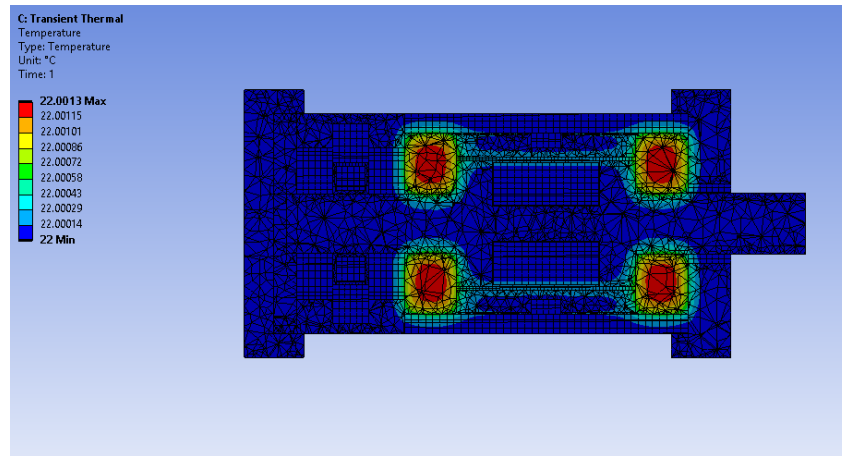


Figure 16: Transient Thermal analysis.

4.3 Optimization

Computer-aided simulation tools have enabled engineers to design highly complex systems while taking into consideration constraints across multiple physical domains (e.g., mechanical, electronic, thermal, etc.) (Irina 2014). Optimization is an effective technique to identify the important design parameters and subsequently search for their optimal values.

Section 4.1 indicates that D and $\zeta_{viscous}$ are both functions of h , L_a , and L_p . In this study, the following parameters, h , L_a , and L_p must be optimized to give the desired design requirements. A multi-objective optimization program is developed in ANSYS platform to carry out such a comprehensive optimization study as shown in Figure 17. Maxwell, Transient Thermal, and Microsoft Excel modules are run simultaneously to determine the magnetic flux density in the flow gap, to calculate D and $\zeta_{viscous}$.

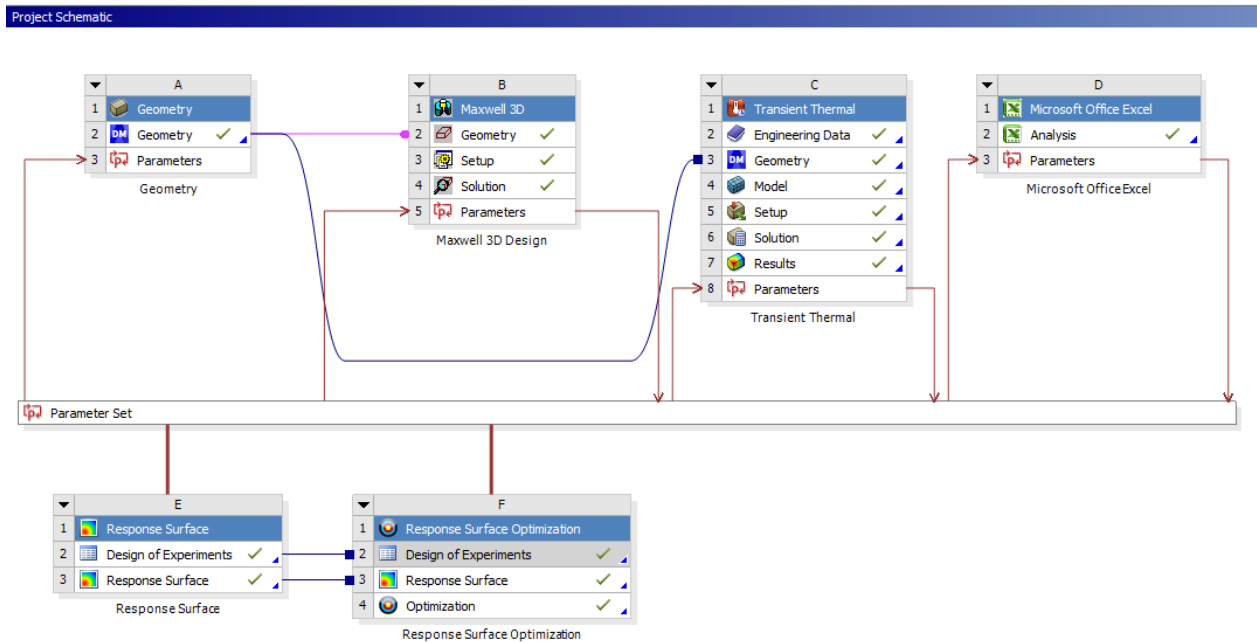


Figure 17: A multi-objective optimization program developed in ANSYS platform.

The input and output parameters are stored in the Microsoft Excel module, which is connected with the “parameter set” in Ansys workspace, as shown in Figure 18. The geometric parameters are linked with the Geometry module, while the current input to the coils is fed to the Maxwell module. A large number of equations from sections (3.2) and (3.3) are all entered in the Microsoft Excel module (e.g., dynamic range, D , viscous damping force, F_{viscous} , controllable MR damping force, F_{MR} , yield stress, τ , viscous damping ratio, ζ_{viscous} , as well as, the total viscous heating, W_{total}). The outputs of the Maxwell module, *i.e.*, magnetic flux density, B , and magnetic field intensity, H , are passed to the Microsoft Excel module to calculate, $\tau(B)$; thus, F_{MR} and W_{total} .

W_{total} is transferred to the Transient Thermal module as a heat source to the MR fluid. Likewise, another output of the Maxwell module, total Ohmic loss, is linked to the Transient Thermal module directly as the other heat source to the coils.

In addition, all circuits suffer from some form of time delay between the input and output terminals when voltage is continuously applied; hence, the electromagnet's time constant was optimized as well. These communications between the modules are performed simultaneously. Then, the optimum design is explored with the response surface optimization module. Figure 18 and Figure 19 show the optimized input and output parameters, respectively.





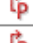





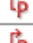


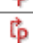




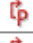
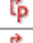
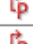
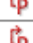
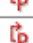
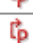




Outline of All Parameters				
	A	B	C	D
1	ID	Parameter Name	Value	Unit
2	[-] Input Parameters			
3	[-]  Geometry (A1)			
4	 P90	DS_al	0.015	m
5	 P91	DS_h	0.0015	m
6	 P92	DS_L1	0.022	m
7	 P93	DS_L2	0.022	m
8	 P94	DS_pL	0.045	m
9	[-]  Maxwell 3D Design (B1)			
10	 P100	\$Temp [cel]	295.15	K
11	 P142	\$ElectricCurrent [A]	1000	A
12	[-]  Transient Thermal (C1)			
13	 P168	MRF Magnitude	4578.1	W m ⁻³
14	 P169	Coil Magnitude	1.0497	W m ⁻³
15	[-]  Microsoft Office Excel (D1)			
16	 P106	WB_AWG	21	
17	 P107	WB_B_ave	0.11886	T
18	 P112	WB_CoilHeight	0.018	m ▾
19	 P114	WB_ConductorSource	1000	A ▾
20	 P118	WB_frequency_f	4	Hz ▾
21	 P120	WB_h	0.0015	m ▾
22	 P121	WB_HMRF	14869	A m ⁻¹
23	 P122	WB_L_1	0.022	m ▾
24	 P123	WB_L_2	0.022	m ▾
25	 P124	WB_L_a	0.015	m ▾
26	 P125	WB_L_p	0.045	m ▾
27	 P128	WB_R_p	0.03731	m ▾
28	 P131	WB_Stroke_X	0.00635	m ▾
29	 P132	WB_Temp	22	C ▾
*	 New input parameter	New name	New expression	

Figure 18: Optimization input parameters.

31	Output Parameters			
32	Maxwell 3D Design (B1)			
33	P96	AvgMag_B1	0.081327	
34	P97	AvgMag_B3	0.15639	
35	P101	H1	10174	
36	P102	H2	19564	
37	P103	OhmicLoss	1.0497	
38	Transient Thermal (C1)			
39	P170	Temperature Maximum	22.001	C
40	P171	Max Temp in MRF Maximum Temperature	22.001	C
41	P172	Max Temp in Coil Maximum Temperature	22	C
42	Microsoft Office Excel (D1)			
43	P108	WB_C_th	0.008	m
44	P109	WB_Ceq	2755.3	N s m ⁻¹
45	P110	WB_Ceq_total	6381.7	N s m ⁻¹
46	P111	WB_CoilArea	0.00081	m ²
47	P113	WB_CoilResistance	8.7566	Ohm
48	P115	WB_CurrentInput	0.84631	A
49	P116	WB_D	2.8192	
50	P126	WB_mu	0.15795	Pa s
51	P127	WB_PowerInput	6.2718	W
52	P133	WB_Turns	1181.6	
53	P135	WB_Velocity_V0	0.15959	m s ⁻¹
54	P136	WB_VoltageInput	7.4108	V
55	P137	WB_W_total	20.318	J
56	P138	WB_W_viscous	8.772	J
57	P139	WB_zi_total	0.013394	
58	P140	WB_zi_viscous	0.0057825	
59	P141	WB_tau	4491.4	Pa
60	P165	WB_V_chamber	0.017752	m ³
61	P166	WB_A_p	0.0043732	m ²
*	New output parameter		New expression	

Figure 19: Optimization output parameters.

The optimization algorithm provides several candidates. In this approach, the local optima in each objective are obtained and modified to create a new population of candidate designs. The significant input and output values obtained from the analysis to optimize the dynamic range and viscous damping ratio response are provided in Table 2.

Table 2: Obtained optimized input and output parameters

Input parameter Name	Best candidate
h (m)	0.001500773
L_a (m)	0.019584297
L_p (m)	0.046805543
Stroke_X (m)	0.006755364

Output parameter Name	Best candidate
Dynamic range, D ,	3.120488218
Viscous damping force, F_{viscous} (N)	1083.504163
MR damping force, F_{MR} (N)	769.2043897

CHAPTER 5

SUMMARY AND CONCLUSIONS

5.1 Conclusion

In this study, a novel semi-active vibration isolation system called Magnetorheological-based Semi-Active Vibration Isolator (MR-SAVI for short) was proposed to potentially attenuate the deteriorating effects of the external vibrations on the quality of the 3D printed parts on shipboard. For the design of MR-SAVI, a comprehensive modeling approach, including both the analytical and simulation modeling, was presented. The analytical modeling included parameters that required computer simulations, such as electromagnetic and thermal analyses. A primitive way of tackling this challenge would be performing the simulations on an FEA software and then inputting the results of these simulations into the analytical formulations on different software such as Excel or MATLAB and carrying out the analytical calculations on that different platform, and vice versa. However, this would be a very cumbersome process and hinder the process of identifying the relationships between the many parameters in the analytical formulations thoroughly. Rather, we preferred to develop a comprehensive program on a single platform, where we could connect the FEA simulations directly with the analytical formulation and allow them to communicate with each other simultaneously. To do that, we used Ansys. This also allowed us to perform subsequent optimization studies within the same platform conveniently. With the help of this Ansys program, we were able to obtain the optimal values of the significant design parameters.

The generic method presented here can be conveniently used for future MR-SAVI designs with different design requirements.

5.2 Future work

Further study can be done by testing and characterizing MREs and validating the 3D printing method for MREs fabrication.

Fabricating, building, and testing MR-SAVI. Experimental validation of the optimization results will give more opportunities for data acquisition, which can be analyzed, and to further examine the accuracy of the analytical and FE model.

REFERENCES

- Rayna, Thierry, and Ludmila Striukova. 2014. "The Impact of 3D Printing Technologies on Business Model Innovation." In *Digital Enterprise Design & Management*, 119–132. Springer from https://link.springer.com/chapter/10.1007/978-3-319-04313-5_11.
- R Rayna, Thierry, Ludmila Striukova, and John Darlington. 2015. "Co-Creation and User Innovation: The Role of Online 3D Printing Platforms." *Journal of Engineering and Technology Management* 37: 90–102 from <https://doi.org/10.1016/j.jengtecman.2015.07.002>.
- Ayna, Thierry, Ludmila Striukova, and John Darlington. 2015. "Co-Creation and User Innovation: The Role of Online 3D Printing Platforms." *Journal of Engineering and Technology Management* 37: 90–102 from <https://doi.org/10.1016/j.jengtecman.2015.07.002>.
- Grant, Thomas Grant. "Why Do Buildings Collapse in an Earthquake, and How Can It Be Prevented?" *Pdf-Civil-Engineering.*, Jan. 2020
- Ali, Sk Faruque, and Ananth Ramaswamy. 2009. "Testing and Modeling of MR Damper and Its Application to SDOF Systems Using Integral Backstepping Technique." *Journal of Dynamic Systems, Measurement and Control, Transactions of the ASME* 131 (2): 1–11. <https://doi.org/10.1115/1.3072154>.
- Banjanin, Bojan, Gojko Vladić, Magdolna Pál, Vladimir Dimovski, Savka Adamović, and Gordana Delić. 2018. "Production Factors Influencing Mechanical and Physical Properties of Fdm Printed Embossing Dies," 225–36. <https://doi.org/10.24867/grid-2018-p28>.

- Bastola, A. K., V. T. Hoang, and L. Li. 2017. "A Novel Hybrid Magnetorheological Elastomer Developed by 3D Printing." *Materials and Design* 114 (January): 391–97. <https://doi.org/10.1016/j.matdes.2016.11.006>.
- Bastola, A. K., M. Paudel, and L. Li. 2018. "Development of Hybrid Magnetorheological Elastomers by 3D Printing." *Polymer* 149 (August): 213–28. <https://doi.org/10.1016/j.polymer.2018.06.076>.
- Behrooz, Majid, Xiaojie Wang, and Faramarz Gordaninejad. 2014. "Performance of a New Magnetorheological Elastomer Isolation System." *Smart Materials and Structures* 23 (4). <https://doi.org/10.1088/0964-1726/23/4/045014>.
- Cesmeci, Sevki, Faramarz Gordaninejad, Keri L. Ryan, and Walaa Eltahawy. 2019. "Design of a Fail-Safe Magnetorheological-Based System for Three-Dimensional Earthquake Isolation of Structures." *Mechatronics* 64 (December). <https://doi.org/10.1016/j.mechatronics.2019.102296>.
- Clarke, C. S.J., R. Buchanan, M. Efthymiou, and C. Shaw. 2005. "Structural Platform Solution for Seismic Arctic Environments-Sakhalin II Offshore Facilities." *Proceedings of the Annual Offshore Technology Conference* 2005-May: 1062–82.
- Dong, Xiao Min, Miao Yu, Chang Rong Liao, and Wei Min Chen. 2009. "A New Variable Stiffness Absorber Based on Magneto-Rheological Elastomer." *Transactions of Nonferrous Metals Society of China (English Edition)* 19 (SUPPL. 3). [https://doi.org/10.1016/S1003-6326\(10\)60118-5](https://doi.org/10.1016/S1003-6326(10)60118-5).
- Dyke, S. J., B. F. Spencer, M. K. Sain, and J. D. Carlson. 1996. "Modeling and Control of Magnetorheological Dampers for Seismic Response Reduction." *Smart Materials and Structures* 5 (5): 565–75. <https://doi.org/10.1088/0964-1726/5/5/006>.

- Eski, İktbal, and Şahin Yıldırım. 2009. "Vibration Control of Vehicle Active Suspension System Using a New Robust Neural Network Control System." *Simulation Modelling Practice and Theory* 17 (5): 778–93. <https://doi.org/10.1016/j.simpat.2009.01.004>.
- Hayashikawa, Toshiro, Yoshitaka Matsui, and Takakichi Kaneko. 2000. "Nonlinear Dynamic Behavior and Seismic Isolation of Steel Towers of Cable-Stayed Bridges Under Great Earthquake." *12th WCEE*, 1–9.
- Vicki, Vicki V. May. "Why Do Buildings Collapse in an Earthquake, and How Can It Be Prevented?" *Pdf-Civil-Engineering.*, April 2018.
- Kallio, M., T. Lindroos, S. Aalto, E. Järvinen, T. Kärnä, and T. Meinander. 2007. "Dynamic Compression Testing of a Tunable Spring Element Consisting of a Magnetorheological Elastomer." *Smart Materials and Structures* 16 (2): 506–14. <https://doi.org/10.1088/0964-1726/16/2/032>.
- Kavlicoglu, Barkan, Yanming Liu, Bryce Wallis, Huseyin Sahin, Michael McKee, and Faramarz Gordaninejad. 2020. "Two-Way Controllable Magnetorheological Elastomer Mount for Shock and Vibration Mitigation." *Smart Materials and Structures* 29 (2). <https://doi.org/10.1088/1361-665X/ab4223>.
- Kobori, T. 2000. "Future Perspective of Structural Control in Earthquake Engineering." *Proc. 12th World Conference on Earthquake Engineering, Auckland, New Zealand Paper No.:* 1–4.
- Kunde, MC, and RS Jangid. 2003. "Seismic Behavior of Isolated Bridges: A-State-of-the-Art Review." *Electronic Journal of Structural Engineering* 3 (2): 140–69.
- Kwon, Seung Hyuk, Jin Hyun Lee, and Hyoung Jin Choi. 2018. "Magnetic Particle Filled Elastomeric Hybrid Composites and Their Magnetorheological Response." *Materials* 11 (6): 1–22. <https://doi.org/10.3390/ma11061040>.

- Li, Guojie, and Ze Biao Yang. 2020. "Modelling and Analysis of a Magnetorheological Damper with Nonmagnetized Passages in Piston and Minor Losses." *Shock and Vibration* 2020. <https://doi.org/10.1155/2020/2052140>.
- Li, Hongnan, and Linsheng Huo. 2010. "Advances in Structural Control in Civil Engineering in China." *Mathematical Problems in Engineering* 2010. <https://doi.org/10.1155/2010/936081>.
- Li, Hongqi, Chaochao Yu, Rui Chen, Juan Li, and Jinxing Li. 2012. "MR Fluid Damper and Its Application to Force Sensorless Damping Control System." *Colloids and Surfaces A: Physicochemical and Engineering Aspects* 395: 116–24. <https://doi.org/10.1016/j.colsurfa.2011.12.014>.
- Li, Yancheng, Jianchun Li, Weihua Li, and Haiping Du. 2014. "A State-of-the-Art Review on Magnetorheological Elastomer Devices." *Smart Materials and Structures*. Institute of Physics Publishing. <https://doi.org/10.1088/0964-1726/23/12/123001>.
- Mil-std. 2005. "Test Method Standard Mechanical Vibrations of (Type I – Environmental and Type II – Internally Excited)." Vol. 1.
- Poynor, James C, and Charles Reinholtz. 2001. "Innovative Designs for Magneto-Rheological Dampers." *Expedition*, 1–12.
- Sahin, Ismail, Sevki Cesmeci, and Norman M. Wereley. 2011. "Sensitivity of Magnetorheological Damper Behavior to Perturbations in Temperature via Bouc - Wen Model." In *Electro-Rheological Fluids and Magneto-Rheological Suspensions -Proceedings of the 12th International Conference*. https://doi.org/10.1142/9789814340236_0091.
- Soong, T T, and B F Spencer. 2000. "ACTIVE , SEMI-ACTIVE AND HYBRID CONTROL OF STRUCTURES ! (T) + C X ! (T) + Kx (t) = Du (t) + Ef (t) M ! X." *I2Wcee2000* 33 (3): 1–16.

- Spaggiari, A. 2012. "Properties and Applications of Magnetorheological Fluids." *Frattura Ed Integrità Strutturale* 23: 57–61. <https://doi.org/10.3221/IGF-ESIS.23.06>.
- Swevers, J., C. Lauwerys, B. Vandersmissen, M. Maes, K. Reybrouck, and P. Sas. 2007. "A Model-Free Control Structure for the on-Line Tuning of the Semi-Active Suspension of a Passenger Car."
- Tip, Earthquake. 2003. "How Flexibility of Buildings Affects Their Earthquake Response?" *Indian Concrete Journal* 77 (3): 967–68.
- Vaezi, Mohammad., and Shoufeng Yang. 2014. "3D Printing of Magnetorheological Elastomers (MREs) Smart Materials." *Proceedings of the International Conference on Progress in Additive Manufacturing*, no. May: 139–44. <https://doi.org/10.3850/978-981-09-0446-3>.
- Eltahawy, Walaa, Keri Ryan, Sevki Cesmeçi, and Faramarz Gordaninejad. 2019. "Displacement/Velocity-Based Control of a Liquid Spring—MR Damper for Vertical Isolation." *Structural Control and Health Monitoring* 26 (7): 1–18. <https://doi.org/10.1002/stc.2363>.
- Cesmeçi, Sevki, Faramarz Gordaninejad, Keri L. Ryan, and Walaa Eltahawy. 2018. "A Liquid Spring—Magnetorheological Damper System under Combined Axial and Shear Loading for Three-Dimensional Seismic Isolation of Structures." *Journal of Intelligent Material Systems and Structures* 29 (18): 3517–32. <https://doi.org/10.1177/1045389X18783090>.
- Warn, Gordon P, and Keri L Ryan. 2012. "A Review of Seismic Isolation for Buildings: Historical Development and Research Needs." *Buildings* 2 (3): 300–325. <https://doi.org/10.3390/buildings2030300>.
- Sevenson, Brittney. *U.S. Navy Installs 3D Printer On Their First Ship, The USS Essex*. 23 Apr. 2014, 3dprint.com/2554/uss-essex-3d-printer-navy/.

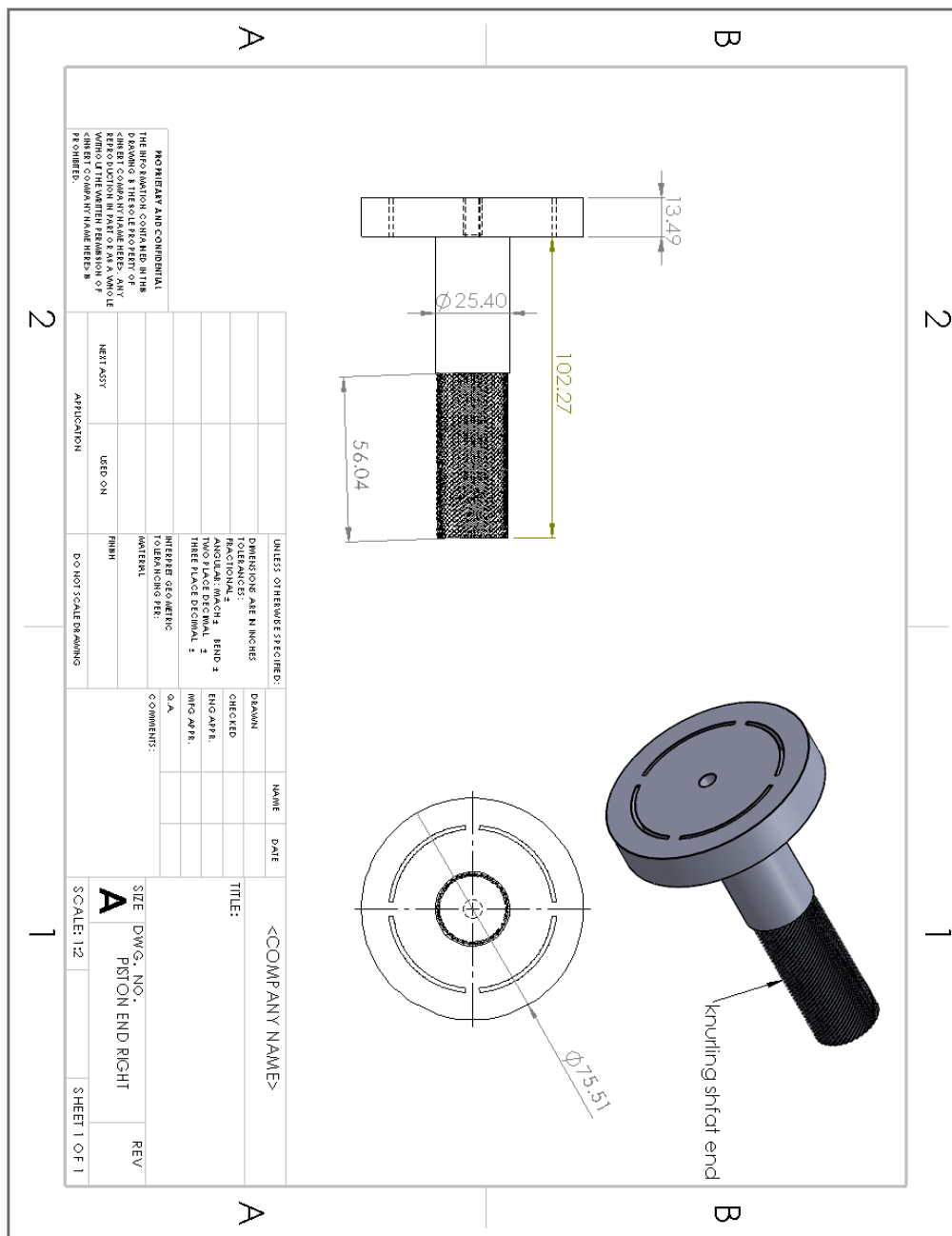
- Cesmeci, Sevki. 2017. "A Fail-Safe, Bi-Linear Liquid Spring, Controllable Magnetorheological Fluid Damper for a Three-Dimensional Earthquake Isolation System" 11 (1): 92–105.
- Irina, Brinster. 2014. "Multi-Objective Algorithms for Coupled Optimization of Mechanical and Electromagnetic Systems" 7 (December): 219–32.
- Delivorias, R.P. 2004. "Research on Smart Materials:"
- Yang, G., B. F. Spencer, J. D. Carlson, and M. K. Sain. 2002. "Large-Scale MR Fluid Dampers: Modeling and Dynamic Performance Considerations." *Engineering Structures* 24 (3): 309–23. [https://doi.org/10.1016/S0141-0296\(01\)00097-9](https://doi.org/10.1016/S0141-0296(01)00097-9).
- Symans, D.M. and Kelly, S.W. (1998). "Hybrid seismic isolation of bridge structure ", Proc. of the Second World Conference on Structural Control, Vol. 2, 923-932.
- Kurata, Narito. 2004. "Actual Seismic Response Control Building with Semi-Active Damper System." *Structures - A Structural Engineering Odyssey, Structures 2001 - Proceedings of the 2001 Structures Congress and Exposition* 109 (June): 1427–47. [https://doi.org/10.1061/40558\(2001\)119](https://doi.org/10.1061/40558(2001)119).
- McKee, Michael, Faramarz Gordaninejad, and Xiaojie Wang. 2018. "Effects of Temperature on Performance of Compressible Magnetorheological Fluid Suspension Systems." *Journal of Intelligent Material Systems and Structures* 29 (1): 41–51. <https://doi.org/10.1177/1045389X17705203>.
- Eltahawy, W., K. L. Ryan, S. Cesmeci, and F. Gordaninejad. 2018. "Control Strategy for Liquid Spring-Mr Damper for Vertical Isolation." 11th National Conference on Earthquake Engineering 2018, NCEE 2018: Integrating Science, Engineering, and Policy 2: 1025–35.

Cesmeci, Sevki, Nicholas L Wilson, Norman M Wereley, and Ismail Sahin. 2010. "Sensitivity of Magnetorheological Damper Behavior to Perturbations in Temperature." <https://doi.org/10.1115/SMASIS2010-3802>.

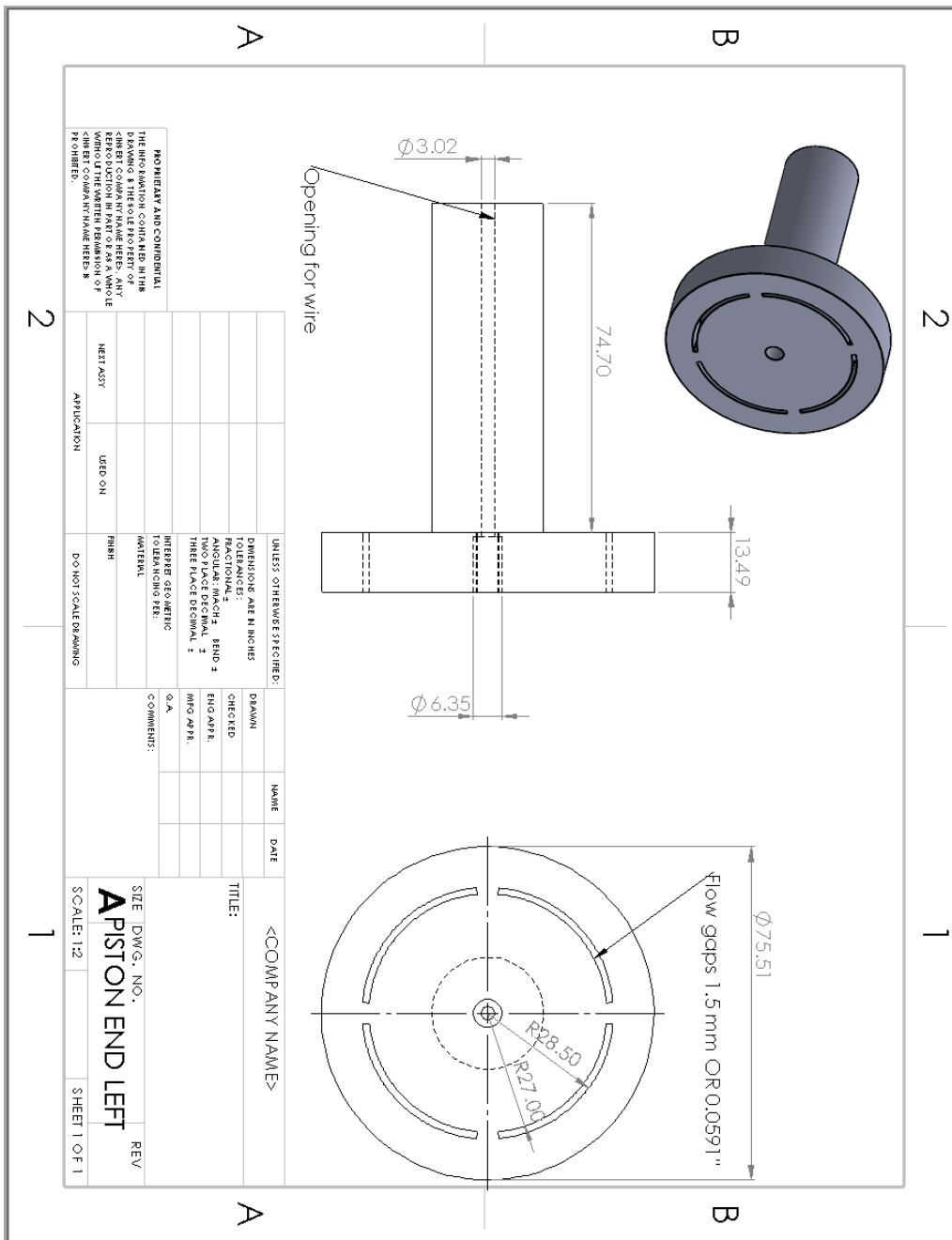
APPENDICES

APPENDIX A. PISTON RIGHT END TECHNICAL DRAWING OF THE MR-SAVI

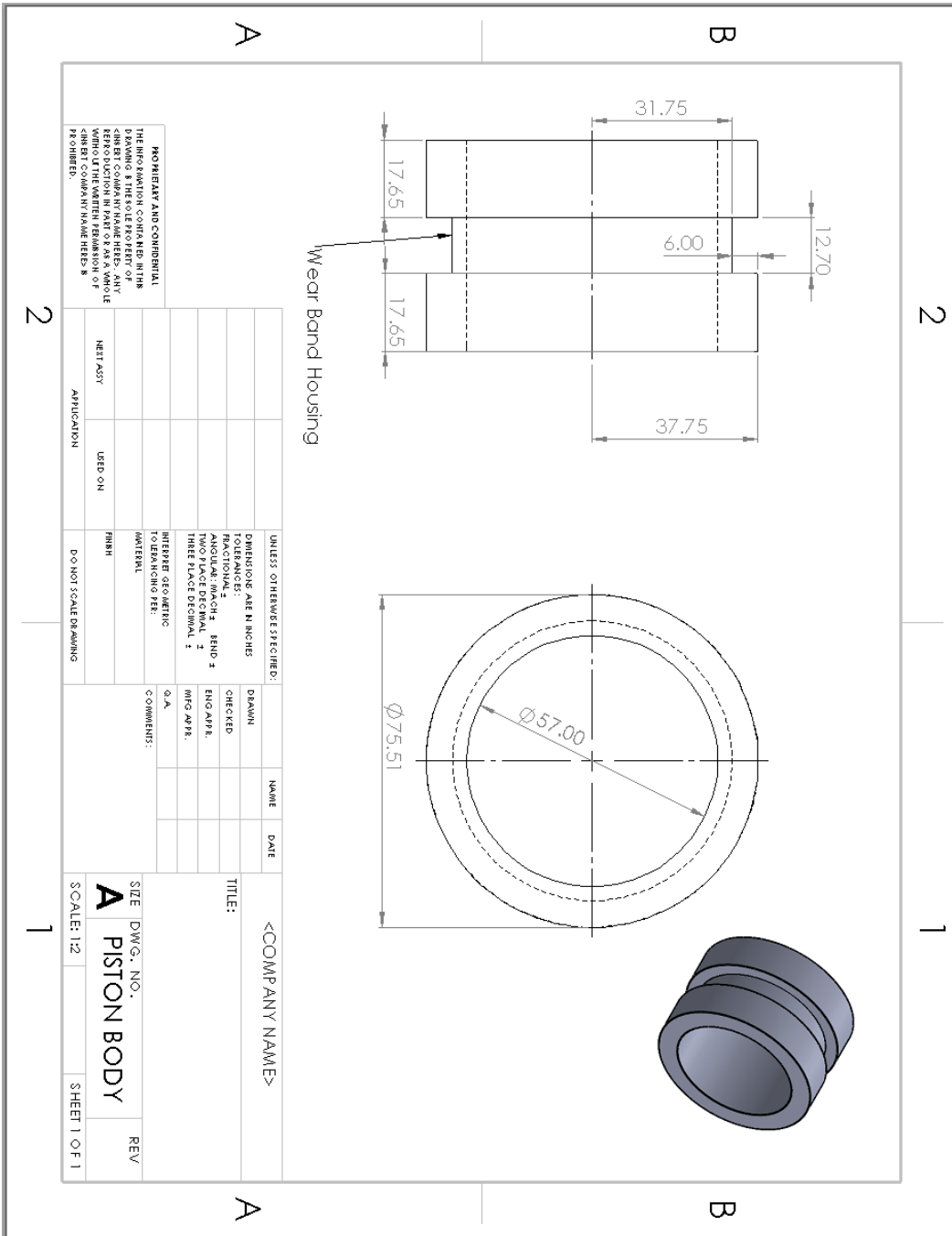
All technical drawings units are in mm.



APPENDIX B. PISTON LEFT END TECHNICAL DRAWING



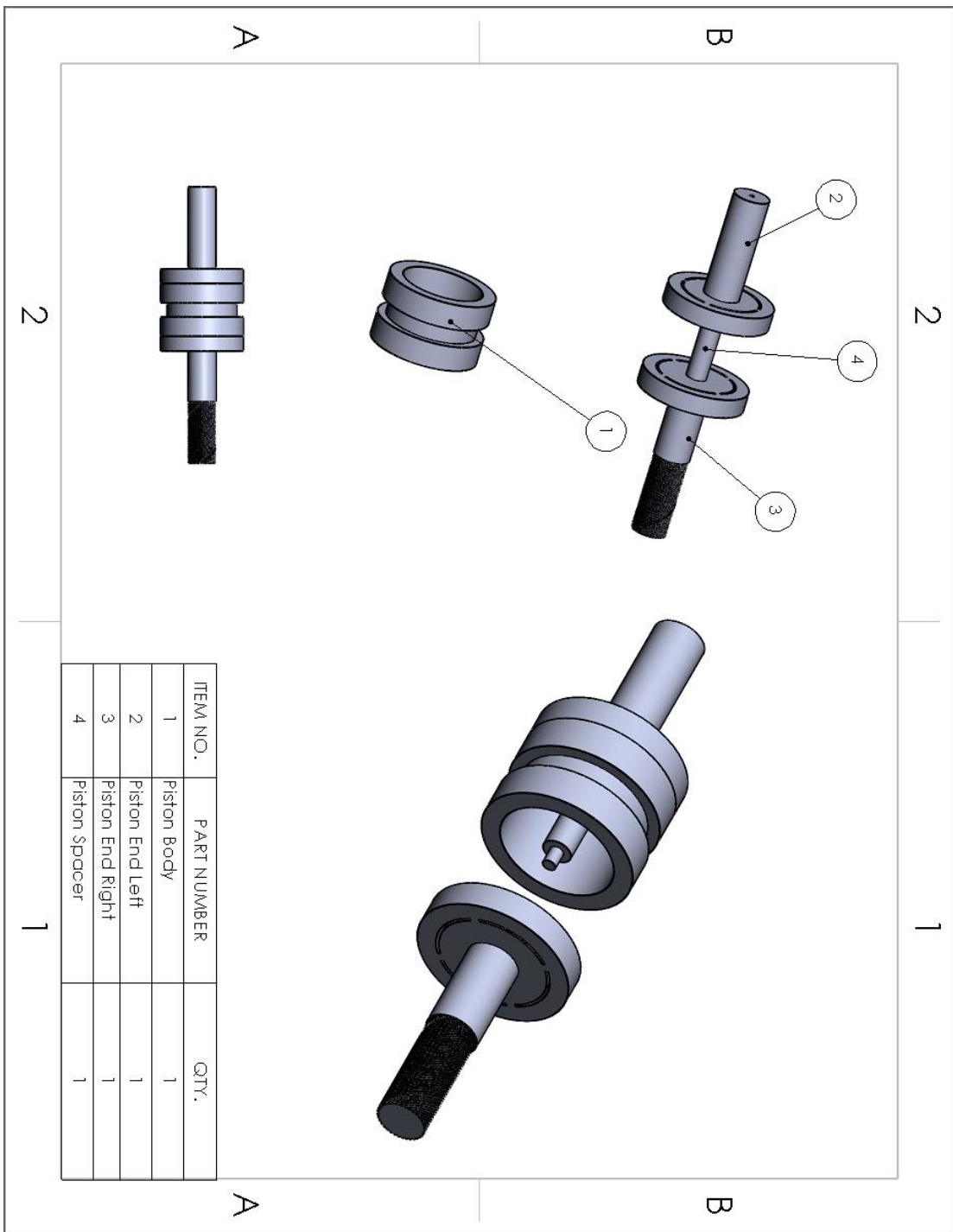
APPENDIX C. PISTON BODY TECHNICAL DRAWING



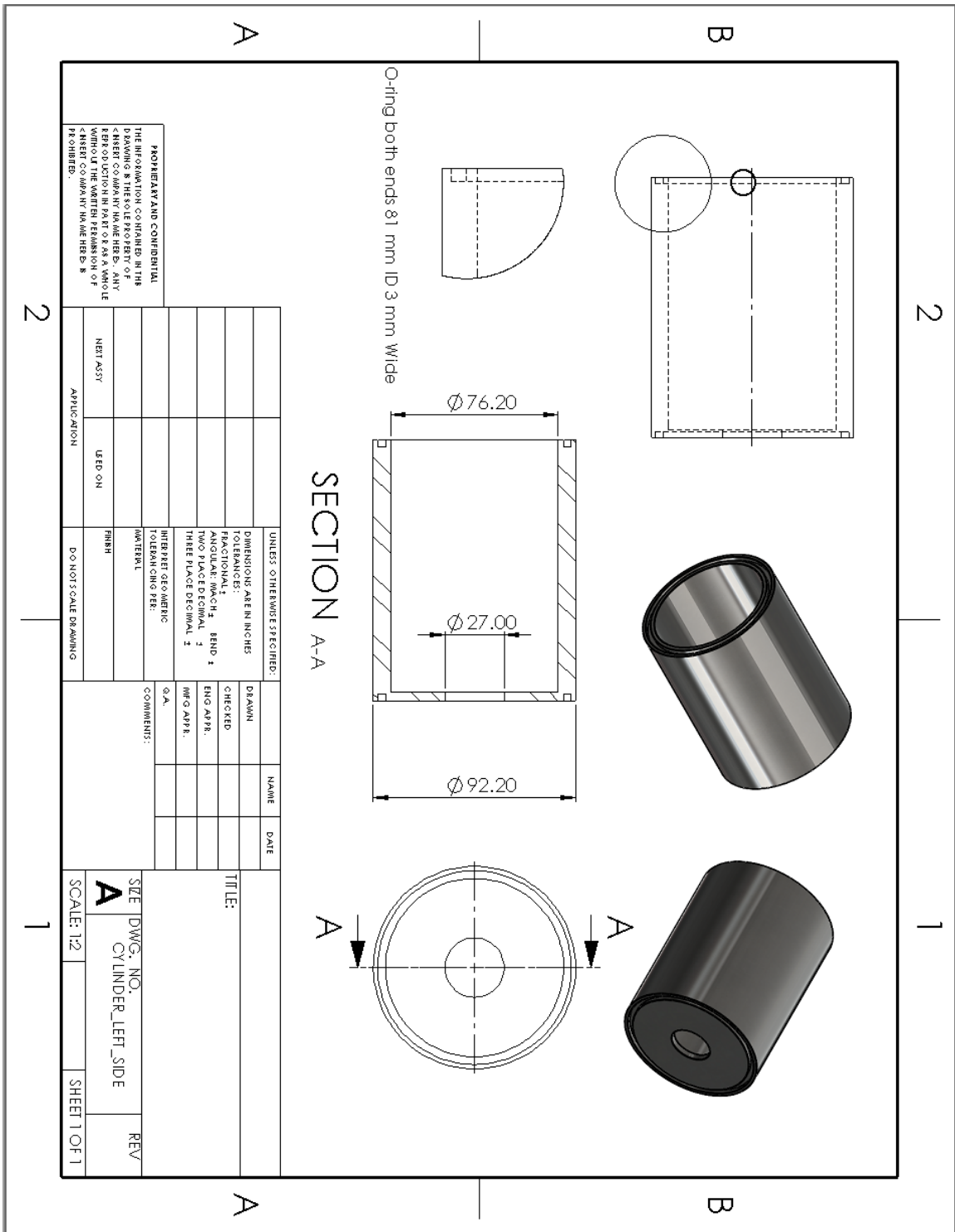
PROPRIETARY AND CONFIDENTIAL
 THE INFORMATION CONTAINED HEREIN IS THE PROPERTY OF <COMPANY NAME> AND IS TO BE KEPT CONFIDENTIAL. REPRODUCTION IN PART OR AS A WHOLE WITHOUT THE WRITTEN PERMISSION OF <COMPANY NAME> IS PROHIBITED.

UNLESS OTHERWISE SPECIFIED:	DRAWN	NAME	DATE	<COMPANY NAME>
DIMENSIONS ARE IN INCHES	CHECKED			TITLE:
TOLERANCES:	ENG APPR.			SIZE DWG. NO.
FRACTIONAL: 1	ENG APPR.			A PISTON BODY
ANGULAR: MACH. BEND 3	Q.A.			SCALE: 1:2
TWO PLACE DECIMAL 2	COMMENTS:			SHEET 1 OF 1
THREE PLACE DECIMAL 3				
INTERPRET GEOMETRIC TOLERANCING PER MATERIAL				
FINISH				
DO NOT SCALE DRAWING				
USED ON				
APPLICATION				
NEXT ASSY				

APPENDIX D. PISTON ASSEMBLY TECHNICAL DRAWING



APPENDIX F. CYLINDER LEFT SIDE TECHNICAL DRAWING



APPENDIX H. CAP RIGHT SIDE TECHNICAL DRAWING

